applied sciences

MDPI

Article

Short- and Long-Term Mechanical and Durability Performance of Concrete with Copper Slag and Recycled Coarse Aggregate Under Magnesium Sulfate Attack

Yimmy Fernando Silva [1,2,*], Claudia Burbano-Garcia [3], Eduardo J. Rueda [1], Arturo Reyes-Román [4] and Gerardo Araya-Letelier [1,2,*]

[1] School of Civil Construction, Faculty of Engineering, Pontificia Universidad Católica de Chile, Santiago 8331150, Chile; eduardo.rueda@uc.cl
[2] Concrete Innovation Hub UC (CIHUC), Faculty of Engineering, Pontificia Universidad Católica de Chile, Santiago 8331150, Chile
[3] Department of Construction Engineering and Management, School of Engineering, Pontificia Universidad Católica de Chile, Santiago 8331150, Chile; cpburbano@uc.cl
[4] Department of Mining Engineering, University of Antofagasta, Antofagasta 1270300, Chile; arturo.reyes@uantof.cl
* Correspondence: yimmy.silva@uc.cl (Y.F.S.); gerardo.araya@uc.cl (G.A.-L.)

Abstract

Sustainability in the construction sector has become a fundamental objective for mitigating escalating environmental challenges; given that concrete is the most widely used man-made material, extending its service life is therefore critical. Among durability concerns, magnesium sulfate ($MgSO_4$) attack is particularly deleterious to concrete structures. Therefore, this study investigates the short- and long-term performance of concrete produced with copper slag (CS)—a massive waste generated by copper mining activities worldwide—employed as a supplementary cementitious material (SCM), together with recycled coarse aggregate (RCA), obtained from concrete construction and demolition waste, when exposed to $MgSO_4$. CS was used as a 15 vol% cement replacement, while RCA was incorporated at 0%, 20%, 50%, and 100 vol%. Compressive strength, bulk density, water absorption, and porosity were measured after water curing (7–388 days) and following immersion in a 5 wt.% $MgSO_4$ solution for 180 and 360 days. Microstructural characteristics were assessed using scanning electron microscopy (SEM), X-ray diffraction (XRD), thermogravimetric analysis with its differential thermogravimetric derivative (TG-DTG), and Fourier transform infrared spectroscopy (FTIR) techniques. The results indicated that replacing 15% cement with CS reduced 7-day strength by $\leq$10%, yet parity with the reference mix was reached at 90 days. Strength losses increased monotonically with RCA content. Under $MgSO_4$ exposure, all mixtures experienced an initial compressive strength gain during the short-term exposures (28–100 days), attributed to the pore-filling effect of expansive sulfate phases. However, at long-term exposure (180–360 days), a clear strength decline was observed, mainly due to internal cracking, brucite formation, and the transformation of C–S–H into non-cementitious M–S–H gel. Based on these findings, the combined use of CS and RCA at low replacement levels shows potential for producing environmentally friendly concrete with mechanical and durability performance comparable to those of concrete made entirely with virgin materials.

Keywords: copper slag; magnesium sulfate; recycled aggregate; compressive strength; microstructural analysis

check for updates

Academic Editor: Muhammad Junaid Munir

Received: 29 June 2025
Revised: 18 July 2025
Accepted: 22 July 2025
Published: 26 July 2025

Citation: Silva, Y.F.; Burbano-Garcia, C.; Rueda, E.J.; Reyes-Román, A.; Araya-Letelier, G. Short- and Long-Term Mechanical and Durability Performance of Concrete with Copper Slag and Recycled Coarse Aggregate Under Magnesium Sulfate Attack. *Appl. Sci.* **2025**, *15*, 8329. https://doi.org/10.3390/app15158329

Copyright: © 2025 by the authors. Licensee MDPI, Basel, Switzerland. This article is an open access article distributed under the terms and conditions of the Creative Commons Attribution (CC BY) license (https://creativecommons.org/licenses/by/4.0/).

1. Introduction

The continuous growth of the world's population, coupled with the accelerated pace of urbanization, has resulted in a substantial increase in global demand for concrete [1]. As the most widely used man-made material and the second-most-consumed material by humans after water, concrete is widely valued for its versatility, satisfactory mechanical performance, ease of molding, and relatively low cost [2–4]. This soaring demand, primarily driven by construction activities, has led to a global production of 4.2 billion tonnes in 2022, with projections indicating that this figure could rise to 5 billion tonnes annually over the next 30 years [5,6]. However, the large-scale production of ordinary Portland cement (OPC), one of the primary components of concrete, is associated with high energy consumption and significant greenhouse gas emissions, contributing approximately 6–8% of global anthropogenic carbon dioxide emissions globally. These CO_2 emissions originate mainly from the combustion of fossil fuels and the decarbonation of limestone ($CaCO_3 \rightarrow CaO + CO_2$) during the clinker production process [7,8]. Additionally, the demolition of buildings at the end of their service life generates considerable amounts of construction and demolition waste (CDW), representing approximately 25–30% of the world's total solid waste [9,10]. A significant fraction of CDW is either landfilled or illegally disposed of in vacant lots, riverbanks, and along roadsides [10–12], leading to severe environmental consequences, such as soil degradation, contamination of rivers and lakes, obstruction of urban drainage systems, and a range of social, economic, and public health issues [13,14].

Accordingly, the construction sector must adopt strategies that curb these environmental impacts to protect natural ecosystems and secure a sustainable future for coming generations. In this context, the development of more sustainable and environmentally friendly concrete—commonly referred to as green concrete—has become a priority [15]. One of the most effective strategies to reduce CO_2 emissions associated with concrete production involves the incorporation of supplementary cementitious materials (SCMs) as partial replacements for Portland cement [15,16]. SCMs not only contribute to the decarbonization of concrete, but also enhance its mechanical performance, increase durability, and reduce production costs [17–19]. Beyond their role in decarbonizing cement production, SCMs improve durability by mitigating deleterious reactions such as alkali–silica reaction (ASR), due to their ability to consume portlandite and limit alkali mobility within the pore solution [20,21]. Commonly used SCMs include fly ash (FA), ground granulated blast furnace slag (GGBS), and silica fume (SF) [19,22–24]. However, growing environmental and supply concerns related to the high demand for cement in concrete production highlight the importance of exploring alternative SCMs. This need has become even more pressing due to the declining availability of fly ash, a widely used SCM, as a result of the global shift away from coal-fired power plants [25]. Among these alternatives, copper slag (CS)—a massive waste of the copper smelting process worldwide—has emerged as a promising candidate, particularly given the rising demand for copper in the context of the global energy transition [26–28]. CS is generated during the copper smelting process in furnaces, with approximately 2.2 to 3 tons of CS produced per tonne of metallic refined copper. Globally, this results in an estimated annual 68.8 million tons produced each year, much of which remains under-utilized. CS is primarily composed of Fe_2O_3, SiO_2, Al_2O_3, and CaO [29–32], with a mineralogical composition mainly consisting of fayalite (Fe_2SiO_4) and magnetite (Fe_3O_4) [33]. Therefore, valorizing this waste in concrete represents a promising and sustainable alternative. While CS has been extensively investigated for its use as aggregates in concrete [31,33–38], its potential as a SCM has received comparatively less attention [28,39,40]. The 15% vol CS replacement level was selected based on prior experimental work [28,41] that identified this dosage as optimal in balancing reactivity,

mechanical performance, and sulfate resistance. Preliminary internal tests also showed that higher CS contents increased early strength loss and plasticity issues, particularly in the presence of RCA.

On the other hand, in response to the challenges associated with CDW, its valorization has been explored as an environmentally driven strategy and, in some cases, an economically viable one. This approach involves the use of appropriate crushing and screening equipment to produce recycled aggregates (RA) for use in the production of mortar, concrete, and pavement base or sub-base layers [10,12,42]. RAs sourced from CDW generally exhibit lower mechanical strength, higher porosity, and greater water absorption compared to natural aggregates (NAs) These limitations are mainly attributed to a weaker interfacial transition zone (ITZ), the presence of microcracks generated during the crushing process, and the residual adhered mortar [43]. For this reason, various international standards have established specific criteria for RAs, considering factors such as their type (originating from concrete, mortar, fired clay bricks, etc.), density, water absorption, and other properties [44,45]. Currently, numerous studies have focused on addressing the limitations of RAs for use in concrete through the application of chemical, mechanical, and thermal treatments, or combinations thereof, and through optimized mixing protocols such as two-stage or pre-saturated mixing [46,47].

Several studies have shown that the mechanical and durability shortcomings of RCA can be mitigated through surface treatments [48,49], pozzolanic coatings [50–52], or pre-saturation technique [53], among others, all of which enhance the interfacial transition zone (ITZ). Concrete's workability and strength can also be improved by optimized mixing protocols that employ stabilizers, water-reducing admixtures, or graded RCA blending [54,55]. These strategies, however, increase processing complexity and cost. Assessing the performance of untreated RCA therefore remains crucial—especially in contexts like Chile, where advanced treatment facilities are often unavailable or economically unfeasible. In this study, RCA is used in its untreated state and combined with CS to establish a practical baseline for their joint behavior in sulfate-rich environments, understanding that this baseline can be further improved with the use of enhanced RCA.

In addition to the responsible use of by-products and waste-derived materials in concrete design, ensuring the long-term durability of this composite material is a key factor for its sustainability. Among the most aggressive environments that can compromise its long-term performance is sulfate attack [56,57]. The external sulfate attack (ESA) results from chemical and physical processes that cause the degradation of concrete's performance [57,58]. When sulfates penetrate the concrete, they react with certain phases formed from the hydration of cement and form ettringite and/or gypsum [59,60], Expansive compounds that cause strains in the concrete, leading to cracking and spalling, which ultimately results in its degradation [61]. One of the most detrimental forms of ESA is caused by magnesium sulfate ($MgSO_4$). In addition to forming gypsum through its reaction with portlandite ($Ca(OH)_2$), it can also produce brucite ($Mg(OH)_2$). Furthermore, $MgSO_4$ attacks calcium silicate hydrates (C–S–H), leading to the formation of magnesium silicate hydrates (M–S–H) that lead to severe cement matrix deterioration, cracking, and weakened ITZs [60,62]. Consequently, it is essential to evaluate the performance of concretes incorporating CS as SCMs and RA as aggregate under ESA; however, to the best of the authors' knowledge, no comprehensive studies have yet examined this combination.

While this study provides valuable qualitative and semi-quantitative microstructural insights into degradation mechanisms, it does not attempt to quantitatively model the relationship between chemical transformations (e.g., M–S–H formation) and mechanical performance loss. Accordingly, this study evaluates the performance of concrete mixtures incorporating CS as a SCM (15 vol%) and recycled coarse aggregate (RCA) derived from CDW as a partial or total replacement of natural coarse aggregate at replacement levels of 0%, 20%, 50%, and 100% by volume. The mixtures were subjected to a 5% magnesium sulfate ($MgSO_4$) solution and cured in water. To assess the behavior of the mixtures under these conditions, visual inspections, compressive strength tests, and microstructural analyses—including scanning electron microscopy (SEM), X-ray diffraction (XRD), and thermogravimetric–differential analysis (TGA)—were conducted.

2. Materials, Mixture Design, and Experimental Methods

2.1. Materials

A general-purpose-type OPC, according to ASTM C150 [63] was used as the primary binder. The CS used as SCM was sourced from a Codelco's Ventanas smelter, Chile, part of the world's largest copper-producing company. Given the coarse particle size of the as-received CS (Figure 1), it was ground to a finer form prior to its use in the mixtures. Table 1 presents the chemical composition of both the OPC and the CS, determined by X-ray fluorescence (XRF). It can be observed that the CS contains significantly higher amounts of Fe_2O_3 and SiO_2 compared to those presented in the OPC. Figure 2 shows the SEM micrographs of OPC and CS particles, revealing angular, irregularly shaped particles with a wide range of sizes.

The fine aggregate used was well-graded river sand with a maximum particle size below 5 mm. It had a fineness modulus of 2.58, a specific gravity of 2.59, and a water absorption of 1.61%. These properties were determined in accordance with ASTM C136 [64] and ASTM C128 [65]. Gravel with a maximum particle size of 12.5 mm was used as the natural coarse aggregate (NCA). The physical properties of NCA included a specific gravity of 2.59 and a water absorption capacity of 1.81%. The RCA with a particle size ranging from 5 to 12.5 mm, obtained from CDW of a university building where the research was conducted, was used to partially or fully replace the NCA. The specific gravity and water absorption values of RCA were 2290 and 7.07%, respectively. These properties of the coarse aggregates were determined in accordance with ASTM C127 [66]. A commercially available superplasticizer (Viscocrete 6000, Sika S.A. Chile, Santiago, Chile) based on polycarboxylates, with a density of 1050 kg/m^3 and a pH between 5 and 6, was used.



Figure 1. CS in its original particle size.

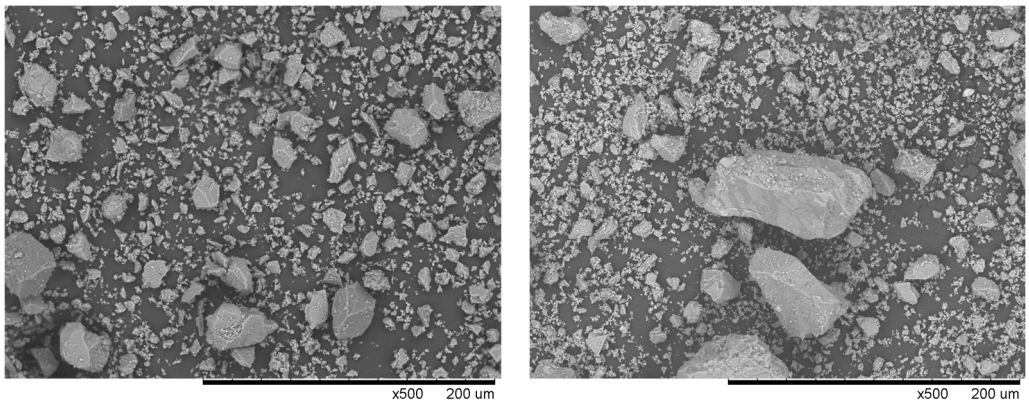

(**a**) (**b**)

Figure 2. SEM images (magnification of 500×): (**a**) OPC and (**b**) CS.

Table 1. Chemical composition of OPC and CS.

Materials	Fe_2O_3	SiO_2	CaO	Al_2O_3	MgO	Na_2O	SO_3	K_2O	LOI
OPC	3.02	19.1	63.34	4.99	1.24	0.79	2.89	0.53	3.66
CS	59.15	29.15	2.84	5.84	1.02	1.02	1.15	1.28	−5.16

2.2. Mixture Design

In the present study, five different concrete mixtures were prepared using a fixed water content (196 kg/m^3). Aggregate moisture corrections were applied individually to account for their distinct absorption capacities. The superplasticizer (SP) dosage was kept constant across all mixtures. The first concrete mixture contained only natural constituents. In the second mixture, 15% of the ordinary Portland cement (OPC) was replaced by copper slag (CS) by volume, while maintaining 100% natural aggregates. The selection of the replacement percentage of OPC with CS was based on previous study, in which the effect of using CS as a supplementary cementitious material (SCM) was evaluated within a replacement range of 0% to 50% [41]. In the remaining three mixtures, natural coarse aggregate (NCA) was partially or fully replaced by recycled coarse aggregate (RCA) at three levels: 20%, 50%, and 100% by volume. The detailed mixture proportions and corresponding mixture identity (IDs) codes are presented in Table 2.

Table 2. Concrete mixture design details.

Mixtures	MIX ID	OPC (kg/m^3)	SC (kg/m^3)	Water (kg/m^3)	NFA (kg/m^3)	SP (kg/m^3)	NCA (kg/m^3)	RCA (kg/m^3)
Reference	Ref.	400	0	196	889.9	2.4	830.9	0
15% CS	M2	340	71.4	196	889.9	2.4	830.9	0
15%CS 20% RCA	M3	340	71.4	196	889.9	2.4	664.7	145.2
15%CS 50% RCA	M4	340	71.4	196	889.9	2.4	415.4	363.1
15%CS 100% RCA	M5	340	71.4	196	889.9	2.4	0	726.2

2.3. Experimental Methods

The experimental program consisted of immersing the different specimens, corresponding to the various mixtures, in a 5% $MgSO_4$ solution to induce sulfate attack, while simultaneously curing them in water for different periods, up to a maximum duration of 360 days. To assess the performance of the mixtures under these aggressive conditions, visual inspections, compressive strength tests, and microstructural analyses were conducted. The latter included XRD, TGA, FTIR and SEM).

After demolding at 23 ± 2 h, all specimens were fully immersed in water at 23 ± 2 °C, consistent with ASTM C192 [67], from demolding until the specified testing age (up to 360 days) to ensure consistent hydration and pozzolanic development.

2.3.1. Visual Inspection

Visual inspection was conducted by analyzing photographic records of 5 × 5 cm cubic specimens corresponding to the different concrete mixtures, captured after 180 and 360 days of exposure. The samples were immersed in a 5% $MgSO_4$ solution, allowing the documentation of surface-level physical changes observed at both exposure durations. These changes included surface disintegration.

2.3.2. Compressive Strength Test

Considering that the mechanical properties of concrete develop continuously, compressive strength was assessed under two different curing regimes: (i) continuous water immersion and (ii) immersion in a 5 wt% $MgSO_4$ solution. For each mixture and test age, three sets of samples were prepared, where each set consisted of three replicate cubes. For the mixtures cured in water, compressive strength was measured at 28, 56, 128, 208, and 388 days. In contrast, for the mixtures exposed to the $MgSO_4$ solution, specimens were initially cured in water for 28 days and then transferred to the sulfate solution. In this case, compressive strength was evaluated after 28, 100, 180, and 360 days of exposure. Compressive strength testing was carried out in accordance with ASTM C39 [68].

2.3.3. Measurement of Water Absorption, Density and Voids

The water absorption, density and voids of the concrete mixtures incorporating CS and varying RCA contents were evaluated in accordance with ASTM C642 [69]. This procedure quantifies open porosity and saturation characteristics, parameters that govern transport phenomena and thus strongly influence long-term durability.

2.3.4. Microstructural Characterization

XRD Analyses

XRD analyses were carried out on representative cement-paste samples composed of either 100% OPC and 85% OPC−15% CS. Samples were extracted after 28 days of curing in water (initial condition) and after 180 days of exposure to a 5% $MgSO_4$ solution. For the analysis, samples of cement paste were pulverized to produce a fine, dry, and homogeneous powder with particle sizes below 75 μm, suitable for XRD testing. This technique enables the qualitative identification of crystalline phases, including primary cement hydration products and secondary compounds related to sulfate attack, such as ettringite, gypsum, or brucite. The objective of this analysis is to assess the mineralogical evolution of the cementitious matrix as a function of binder composition and exposure condition.

TG-DTG Analyses

TG-DTG analysis was employed to monitor the change in mass of the samples as a function of temperature. The experiments were carried out using a TGA Q600 operating under a nitrogen atmosphere to ensure inert testing conditions. The analysis was conducted over a temperature range of 25 °C to 1000 °C, with a constant heating rate of 10 °C/min. Differential thermogravimetric (DTG) curves were obtained by numerically differentiating the TGA signal to resolve overlapping thermal events

FTIR Analyses

FTIR spectral analysis was performed using a Shimadzu IRTracer-100 spectrometer (Shimadzu, Kyoto, Japan) to investigate the microstructural changes in the cementitious pastes. The spectra were recorded in the mid-infrared range from 4000 to 400 cm^{-1}. This analysis aimed to identify functional groups and monitor chemical bond evolution associated with hydration products and possible sulfate-induced phase transformations over time.

SEM Analyses

To investigate the microstructural effects induced by environmental exposure, scanning electron microscopy (SEM) analyses were conducted on the cementitious matrix (cement paste) of the mixtures. Two types of paste samples were prepared: a control paste composed entirely of 100% OPC and a blend containing 15 vol% of CS (85% OPC–15% CS). After 180 days of conditioning in either water or a 5% magnesium sulfate ($MgSO_4$). SEM enables detailed observation of the morphology, distribution, and surface characteristics of hydration products, as well as the identification of degradation features and secondary phases associated with sulfate attack. The analysis focused on detecting microstructural differences attributable to the type of binder and the exposure conditions.

3. Results and Discussion

3.1. Visual Inspections

Figure 3 provides qualitative evidence of surface degradation under magnesium sulfate exposure; however, no quantitative image-based automated analysis [70] (e.g., crack mapping, edge loss quantification) was performed. Future studies should incorporate digital image analysis techniques to quantify degradation metrics, such as surface crack density and erosion index, which would allow for objective comparison between mixtures. The control mixture (M1) exhibited pronounced surface degradation at both 180 and 360 days of exposure. In contrast, the mixtures composed of 85% OPC and 15% CS showed relatively mild deterioration at 180 days. A thin white layer was observed on the surface, attributed to the formation of brucite (magnesium hydroxide), which commonly forms as a result of magnesium sulfate attack [71]. Micro-spectroscopic analyses by Yan et al. [72] have reported that this white surface layer is not only composed of $Mg(OH)_2$, but also contains magnesium carbonate ($MgCO_3$) and magnesium silicate hydrate (M-S(-A)H) phases.

At 360 days, the CS mixtures (M2, M3, M4, and M5) exhibited more pronounced signs of degradation, particularly at the edges of the specimens, with noticeable material loss and possibly a denser white layer. This is attributed to the progressive accumulation of reaction products from the $MgSO_4$ attack, which increases crystallization pressure within the pores. When this internal pressure exceeds the tensile strength of the composite matrix, it triggers cracking and spalling of the mortar [73].

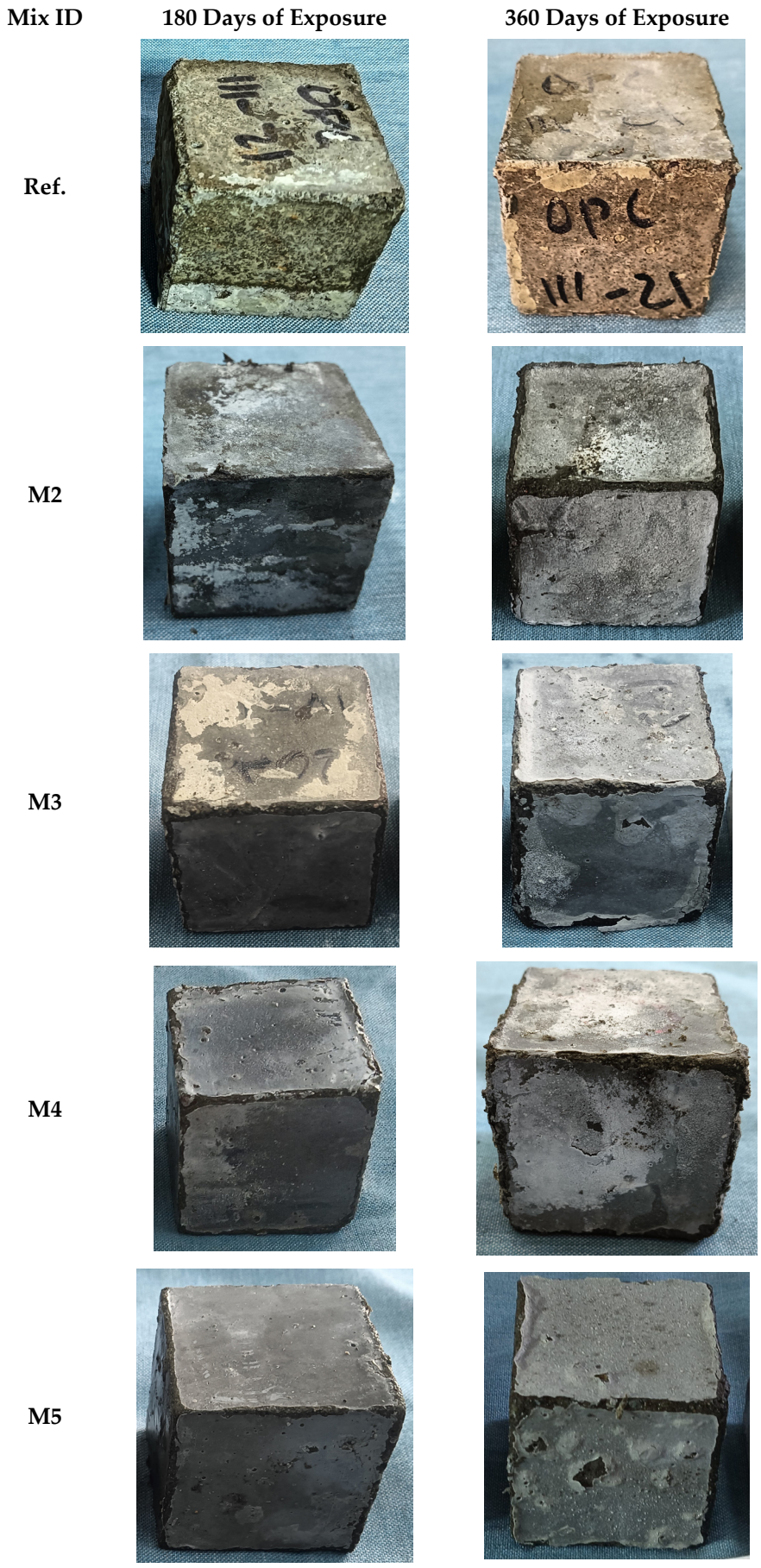

Figure 3. Visual appearance of mixtures exposed in a 5% $MgSO_4$ solution for 180 and 360 days.

3.2. Compressive Strength

The compressive strength was evaluated for concrete mixtures cured in water and exposed to a $MgSO_4$ solution at selected ages, as shown in Figure 4 (where bars indicate mean values, while error bars indicate one standard deviation above and below mean values). Figure 4a shows the results obtained for concretes cured for 28, 56, 128, 128, 208 and 388 days. As expected, an increase in curing age leads to an improvement in the compressive strength of all mixtures. However, this mechanical property decreased monotonically as the RCA content increases, at all curing ages. Specifically, at early curing ages such as 28 and 56 days, when comparing the Ref. mixture (100% virgin materials) with M2 (containing 15% CS as SCM), the compressive strength decreased by 8.44% and 7.78%, respectively. At later curing ages, such as 208 and 388 days, mixture M2 achieved average compressive strengths of 70.62 MPa and 73.62 MPa, respectively. These values were only 5.9% and 4.0% lower than those of the Ref. mixture, indicating a reduced difference in mechanical performance over time. This behavior is attributed to the pozzolanic effect of the CS, which is known to be only moderately reactive and requires extended curing periods for its beneficial effects to become more evident [28,41]. Similar findings were reported by Wang et al. [74], who incorporated CS as SCM in proportions ranging from 10 to 20 wt% for mortar production. Their study showed a reduction in compressive strength at early ages (3, 7, and 28 days), which was attributed to the poor hydrophilicity of the material. This condition increases the amount of free water in the mixture and reduces the formation of hydration products. Despite its lower reactivity compared to OPC, mixtures incorporating up to 15% CS exhibit improved mechanical performance at extended ages [75].

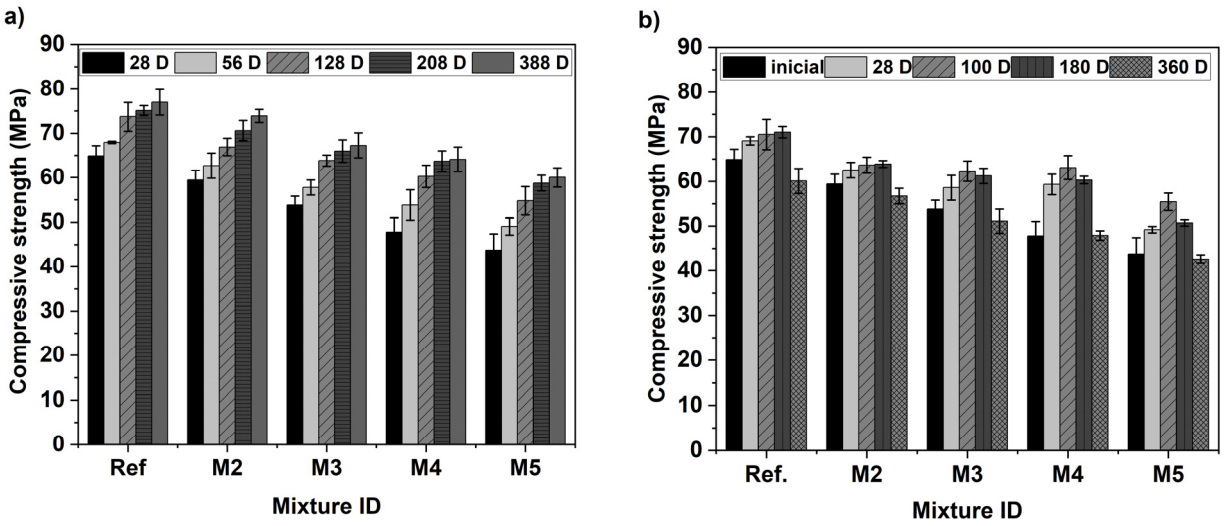

Figure 4. Compressive strength of concretes at different ages: (**a**) cured in water and (**b**) exposed to the 5% $MgSO_4$ solution.

In the case of concretes incorporating RCA (mixtures M3, M4, and M5), at 28 and 56 days of curing, the composite material with the highest content of recycled material, M5 (15% CS and 100% RCA), exhibited average reductions in compressive strength of 32.5% and 27.8%, respectively, compared to the reference mixture, as seen in Figure 4a. The trend remains at 388 days of curing, with reductions of 12.6%, 16.71%, and 22.0% observed in mixtures M3, M4, and M5, respectively, in comparison to the Ref. mixture. The reduction in the mechanical performance of concretes containing recycled concrete aggregates (RCA) has been reported by Silva et al. [12], Joseph et al. [76], Xuyong et al. [77] who attribute this behavior to the presence of adhered mortar. This residual mortar

increases the porosity of the RCA, leading to higher water content in the new interfacial transition zone, which promotes the formation of larger calcium hydroxide (portlandite) crystals, thereby weakening the composite material. Additionally, RCAs may contain microcracks generated during demolition and subsequent crushing and processing stages. It is worth noting that the mechanical performance of the mixture including RCA could be further improved in terms of strength by the use of treated RCA. This inclusion was beyond the scope of this research, and it is recommended as future research.

Figure 4b presents the compressive strength of the mixtures before exposure (i.e., after 28 days of water curing) and after 28, 100, 180, and 360 days of $MgSO_4$ exposure. All mixtures exhibited an initial increase in compressive strength at early exposure ages, followed by a gradual decline in this mechanical property as the exposure time increased. At 28 and 100 days of exposure, all mixtures showed higher compressive strength compared to the strength developed prior to the onset of exposure. This temporary gain is attributed to the formation of expansive substances such as ettringite and gypsum, which fill the concrete's pores and contribute to greater densification [78,79]. At prolonged exposure durations (180 and 360 days), the continued formation of these expansive products induces internal expansion stresses, which in turn promote the development and propagation of microcracks. In addition to this phenomenon, the degradation of the C–S–H phase—through its transformation into M–S–H gel—weakens the binder matrix, ultimately resulting in a loss of mechanical strength [41,78,80]. These effects, corroborated by the surface deterioration documented Figure 3, are ultimately responsible for surface spalling, material loss, and compressive strength reduction.

Figure 5 compares the compressive strength of concretes exposed to the $MgSO_4$ solution with that of their counterparts cured in water, evaluated at the same time intervals from their casting. At 28 days of exposure, no negative effect on the compressive strength of concretes exposed to this aggressive environment is observed; on the contrary, a strength gain is even recorded compared to the specimens cured in water over the same period. However, at 180 and 360 days, the mixtures incorporating recycled concrete aggregate (RCA) (M3, M4, and M5) exhibit the greatest losses in mechanical performance (ranging from 24% to 29%). This reduction is attributed to the fact that, compared to natural aggregate, RCAs contain more potentially weak points that are vulnerable to sulfate attack, such as adhered mortar, higher porosity, and a greater number of interfacial transition zones (ITZs) [81]. In concretes with RCA, three ITZs can be identified: (i) between the NA and the matrix; (ii) between the adhered mortar on the RCA and the matrix; and (iii) within the RCA itself, i.e., at the original aggregate–mortar interface. The highest porosity in concrete is concentrated in the ITZ [82], where Mg^{2+} and $SO_4{}^{2-}$ ions react with $Ca(OH)_2$ and monosulfate, forming ettringite, gypsum, and brucite. Crystallizations of these phases raise pore pressure and accelerate crack propagation [83]. Additionally, sulfate attack in the presence of Mg^{2+} ions not only leads to the formation of brucite, but also of M–S–H, as a result of the substitution of Ca^{2+} ions by Mg^{2+}. This process weakens the material matrix due to the lower cohesion of this compound, resulting in reduced mechanical performance [84].

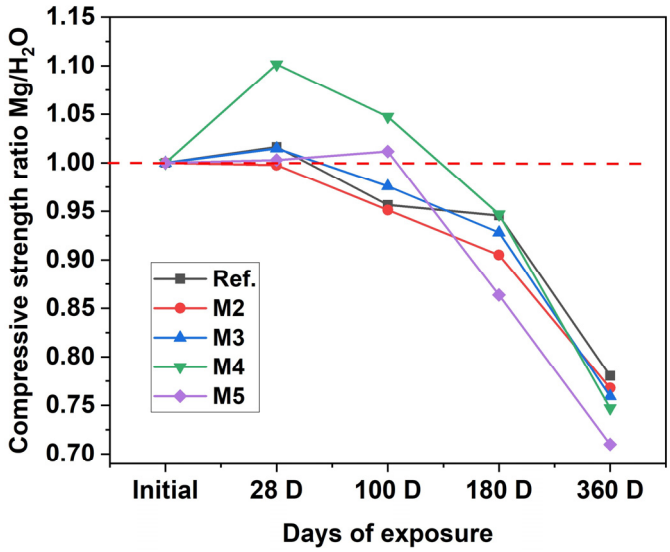

Figure 5. Compressive strength ratio of concretes exposed to $MgSO_4$ and cured in water (Red dashed line indicates equal compressive strength for water curing and sulfate exposure).

3.3. Water Absorption, Density and Voids

Figure 6 presents the bulk density evolution of the concrete mixtures cured in water over hydration time. The Ref. mixture (M1) consistently showed the highest density values, indicating a compact and well-hydrated matrix. In the case of M2, containing 15 vol% CS, a slight reduction in density was observed at early ages (28 days), but the difference narrowed by 180 days and remained small at 360 days. This trend suggests the progressive contribution of the pozzolanic activity of CS to matrix densification, especially at extended curing ages, such as 180 and 360 days, which aligns with that reported in previous studies [4,28,41]. The implemented curing temperature (23 ± 2 °C) was within the optimal range for the progression of pozzolanic reactions, including the slow-reacting phases in CS such as amorphous silicates and aluminates. Prior studies [85] confirm that prolonged curing under these conditions promotes C–S–H formation and densification of the microstructure. Mixtures M2, M3, and M4, combining CS and increasing amounts of RCAs, exhibited a monotonic reduction in density proportional to the RCA content. At 180 days, this reduction was already evident and reflects the influence of RCA's higher porosity and lower specific gravity. The results at 360 days confirm that later hydration stages only partially mitigate the effect of RCA on the bulk density of the concrete mixtures.

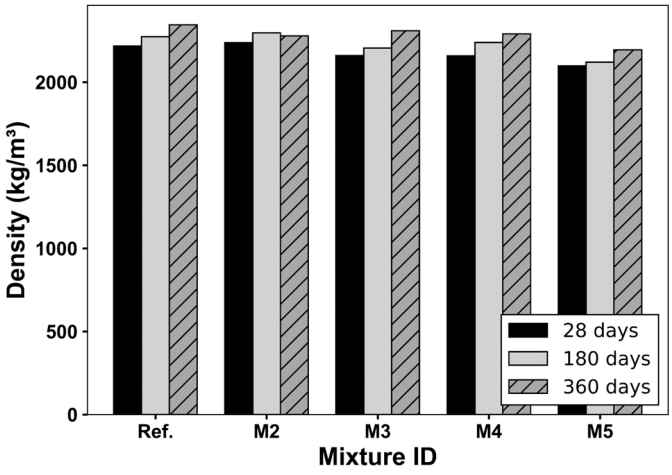

Figure 6. Densities of concrete mixtures at different ages.

Subsequently, Figure 7 shows the water absorption capacity of the mixtures as a function of curing age. Both the Ref. and M2 mixtures exhibit the lowest absorption levels, with very similar values from 180 days onward. This behavior confirms that the replacement of cement by 15% of CS does not negatively affect the permeability of the concrete matrix, and even improves it at extended curing ages, through refinement of the pore structure [28]. In mixtures with RCA and 15% CS (M2–M4), water absorption monotonically increases as the RCA replacement level increases. At 180 days, the differences between the Ref. and 15 CS-RCA-containing mixes were already pronounced, highlighting the persistent influence of RCA's internal porosity; a similar trend was obtained in a previous work [4]. Although some reduction in absorption occurs between 28, 180 days and 360 days, due to ongoing hydration, the improvements are insufficient to compensate for the inherently porous nature of the RCAs [12].

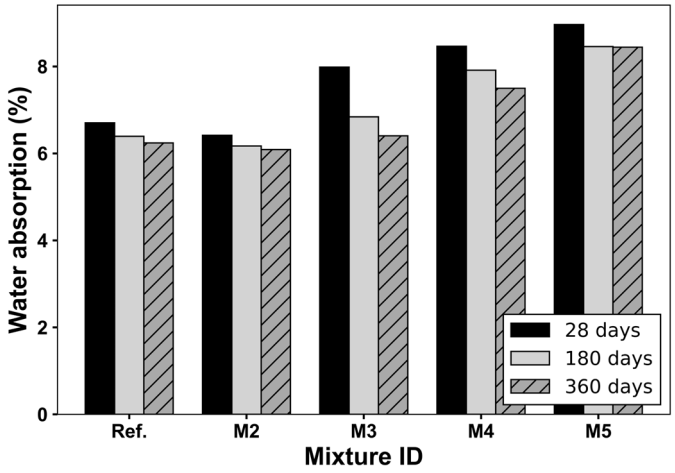

Figure 7. Water absorption (%) of concrete mixtures at different ages.

Finally, Figure 8 displays the void content evolution across curing ages. Ref. and M2 mixtures maintain the lowest void content values at all ages. Notably, at 180 days, the voids in M1 decreased further compared to 28 days, likely due to the delayed formation of additional C–S–H from the reaction of CS. This confirms the interpretation that CS promotes progressive pore filling in extended curing conditions, as reported in previous studies [28,41]. In contrast, mixtures containing 15% CS-RCA (M3–M5) exhibit higher void contents overall, consistent with the increased porosity, microcracking, and heterogeneity of the interfacial transition zone (ITZ) introduced by the RCAs [12]. However, by 360 days, a noticeable reduction in void content (%) is observed in M2 and M3, suggesting that ongoing hydration partially compensates for the microstructural weaknesses introduced by RCAs. Despite this improvement, their void levels remain above those of Ref., though slightly lower than M2, indicating that the combined use of CS and RCAs may promote a viable densification mechanism over time, potentially offsetting some of the drawbacks associated with RCA alone.

Although global voids and water absorption were measured in this study, the pore size distribution and connectivity—which directly influence sulfate ingress kinetics—were not characterized. A multi-scale approach, as demonstrated by Zhu et al. [86] in the context of cementitious sludge stabilization using ternary blends, could provide a more comprehensive understanding of how RCA-induced pore network heterogeneity impacts durability.

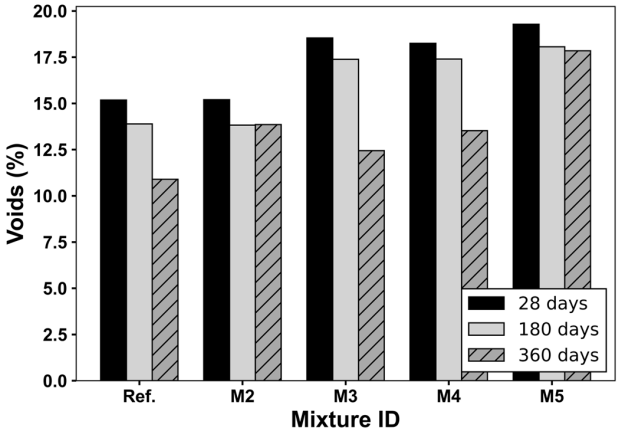

Figure 8. Voids (%) of concrete mixtures at different ages.

3.4. Microstructural Analysis

3.4.1. XRD Analyses

Figure 9 shows the XRD patterns of mixtures containing 100% OPC and 15 vol% CS, collected after 28 days of water curing (initial condition) and after 180 days of exposure to a $MgSO_4$ solution. In Figure 9a, distinct diffraction peaks corresponding to portlandite (CH), ettringite (E), albite (A), belite (B), and mayenite (N) are observed before the sulfate exposure. A and B are unhydrated clinker phases, while E (AFt) and CH are typical hydration products. At 180 days of exposure, a decrease in the intensity of the CH peaks was observed, suggesting the consumption of this phase for the generation of AFt and gypsum. This behavior was also observed by Wang et al. [78], who reported a decrease in CH peaks and an increase in peaks corresponding to ettringite, gypsum and brucite. This phenomenon was attributed to the consumption of Ca^{2+} induced by the presence of SO_4^{2-}, which favors the formation of gypsum when the mixtures are exposed for prolonged periods in this solution. On the other hand, it should be also emphasized that C–S–H, due to its low crystallinity, is not detected by XRD [73] either before or after exposure.

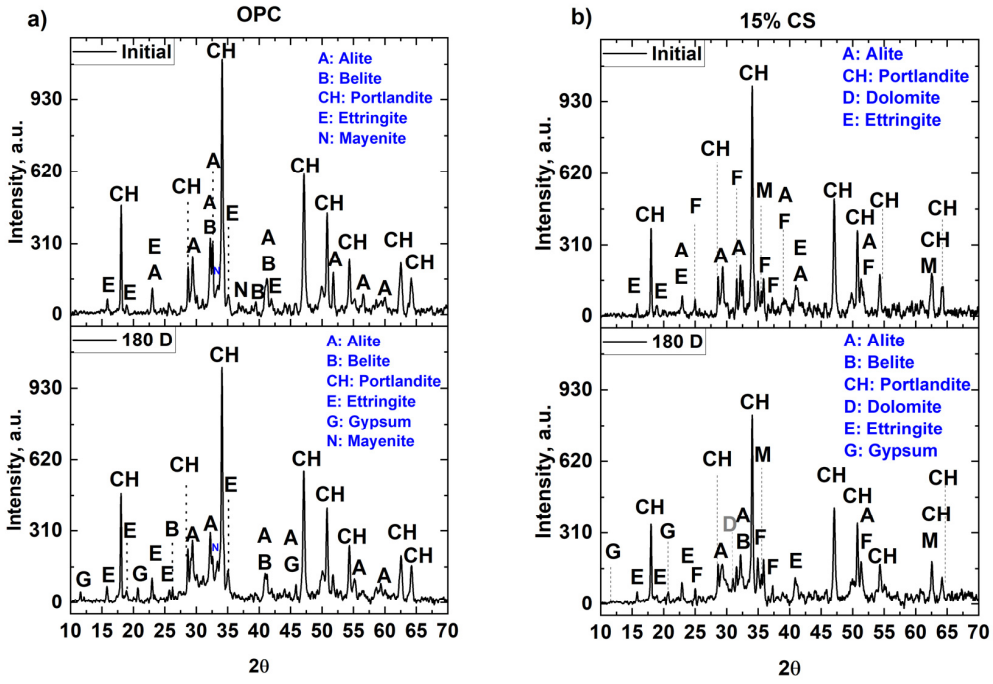

Figure 9. XRD patterns of cementitious matrices with (**a**) 100% OPC and (**b**) 15% CS after 28 days of curing (initial) and 180 days of exposure to $MgSO_4$ solution.

Figure 9b shows the XRD patterns of the mixture containing 15 vol% CS. Characteristic phases of CS, such as fayelite (Fe_2SiO_4) and magnetite (Fe_3O_4), as well as cement hydration products, such as portlandite (CH) and ettringite, are identified in the diffractometric pattern. In addition, a decrease in the intensity of the peaks corresponding to CH is observed, which is attributed to the (i) dilution effect generated by the lower amount of alite and belite phases due to the partial replacement of OPC and (ii) the low initial pozzolanic reactivity of the copper slag [4,41]. At 180 days of exposure, peaks corresponding to gypsum were identified, suggesting that the SO_4^{2-} ions initially reacted with the CH to form gypsum [87], partially consuming this compound, evidenced by the decrease in the intensity of the peaks of this phase when compared to the pre-exposure (initial) diffractogram.

3.4.2. TG-DTG Analyses

Figure 10 presents the TG and DTG curves for Ref. and 15 vol% CS after 28 days of water curing, while Figures 11 and 12 show the TG and DTG curves for the same mixtures after 180 and 360 days of exposure to either water or a 5% magnesium sulfate ($MgSO_4$) solution, respectively.

Figure 10a shows that the total mass loss between 50 and 1000 °C was approximately 22.7% for Ref. in water and 19.9% for 15% CS in water, confirming a lower degree of hydration in the CS-blended cement at early ages. This fact is consistent with the lower initial reactivity of CS, which delays the formation of hydration products compared to a pure Portland cement. In the DTG curve (Figure 10b), the first endothermic peak located between 80 and 200 °C is associated with the dehydration of C-(A)-S-H gel, ettringite (E), and AFm phases, as reported by Lothenbach et al. [88]. The mass loss in this region was approximately 10.4% for Ref. W and 9.3% for 15% CS W, indicating that the CS-blended cement produces fewer early-age hydration products. This result corroborates the findings of Silva et al. [41], who observed reduced chemically bound water and fixed-lime contents were reported for cement blends containing 20% of CS at 28 days.

The second peak, observed between 400 and 500 °C, is associated with the dihydroxylation of portlandite ($Ca(OH)_2$) [89]. The mass loss within this range was approximately 3.6% for Ref. W and 3.3% for 15% CS W. Since CS has been reported to have a pozzolanic contribution at later ages [41], this portlandite reduction is instead associated with a slight dilution effect, in which there are less clinker particles available to react, and form portlandite [89]. The third peak, between 600 and 800 °C, is attributed to the decomposition of calcium carbonate ($CaCO_3$), probably formed due to incipient carbonation during sample preparation.

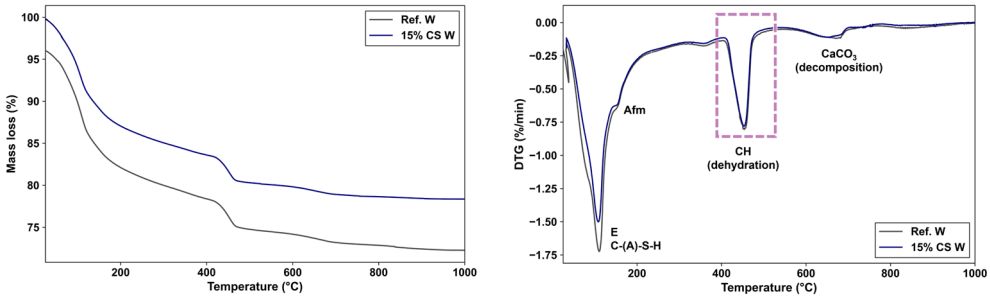

Figure 10. (**a**) TG curves and (**b**) DTG curves of the Ref. and 15% CS for 28 days of curing in water. Before exposure to the $MgSO_4$ solution.

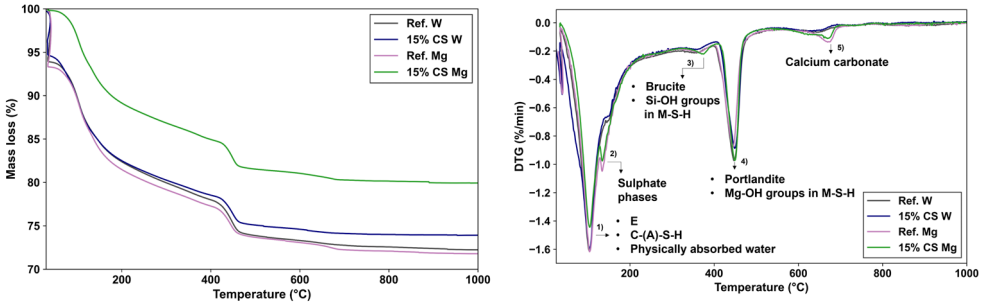

(**a**) (**b**)

Figure 11. (**a**) TG curves and (**b**) DTG curves of the Ref. W and 15% CS W for 180 days exposure to magnesium sulphate. DTG peak: (1) Ettringite (E), Calcium aluminate silicate hydrate (C-(A)-S-H), physically absorbed water; (2) Sulphate phases (Afm phase); (3) Brucite ($Mg(OH)_2$), Magnesium Silicate Hydrate (M-S-H), Si-OH groups; (4) Portlandite ($Ca(OH)_2$), Mg-OH groups in M-S-H; (5) Calcium Carbonate ($CaCO_3$).

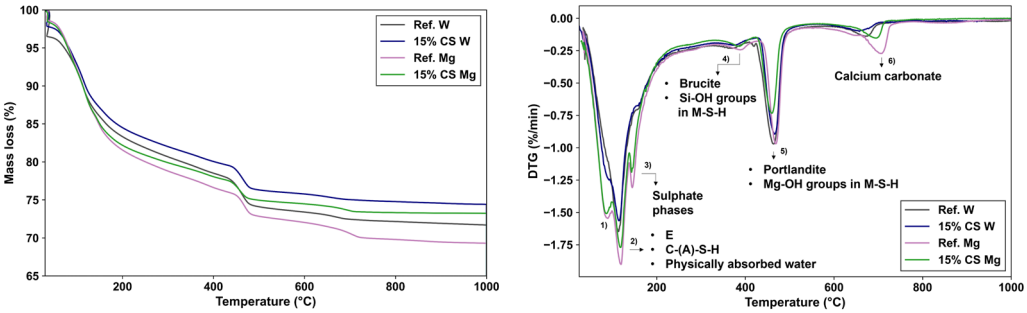

(**a**) (**b**)

Figure 12. (**a**) TG curves and (**b**) DTG curves of the Ref. W and 15% CS W for 360 days exposure to magnesium sulphate. DTG peak: (1) dehydration of the hydration products (e.g., C-S-H); (2) Ettringite (E), Calcium aluminate silicate hydrate (C-(A)-S-H), physically absorbed water; (3) Sulpahe phases (AFm phase); (4) Brucite ($Mg(OH)_2$), Magnesium Silicate Hydrate (M-S-H), Si-OH groups; (5) Portlandite ($Ca(OH)_2$), Mg-OH groups in M-S-H; (6) Calcium Carbonate ($CaCO_3$).

Compared to 28-day results, in Figure 11a,b, Ref. and 15% CS mixtures cured in water exhibit an increase in total mass loss, indicating continued hydration over time. Moreover, the difference between Ref. W and 15% CS W is significantly reduced, which confirms the pozzolanic contribution of CS at extended curing times.

In the TG curve, Figure 11a, the total mass loss between 50 and 1000 °C reaches approximately 21.5% for Ref. W and 20.37% for 15% CS W, reducing the gap observed at 28 days. In the first peak observed in the 80–200 °C region, which corresponds to the dehydration of C-(A)-S-H gel and AFt/AFm phases [90], the mass loss values are approximately 9.73% for Ref. W and 9.39% for 15% CS W, reflecting a comparable degree of hydration in the CS-blended cement and Ref. W. Moreover, it is possible to observe for the second peak between 400 and 500 °C, which is associated with the dihydroxylation of portlandite ($Ca(OH)_2$), that portlandite content is 17.52% lower for 15% CS W compared to Ref. W due to its partial consumption by the CS pozzolanic reaction, similar to the obtained by Silva et al. [41] in their previous work. Finally, the peak between 600 and 800 °C associated with the decomposition of calcium carbonate ($CaCO_3$) [88], was nearly identical for both pastes, suggesting carbonation during sample preparation.

However, under $MgSO_4$ exposure, a significant difference emerges between Ref. Mg and 15% CS Mg. The intensity of the C–S–H related peak (a) in 15% CS Mg is notably reduced, which is attributed to the partial conversion of C–S–H into M–S–H due to magnesium-induced decalcification. Since M–S–H is non-cementitious and dehydrates

gradually from 390 to 500 due to its non-crystalline nature, according to the reported by Bernard et al. [91], it does not contribute significantly to the intensity observed in the 80–200 °C region. This transformation may be facilitated due to the lower alkalinity of the CS-blended cement, when portlandite is consumed by the pozzolanic reaction and further depleted by Mg^{2+} and SO_4 ions. In contrast, Ref. Mg maintains a high peak intensity in the same range, similar to that of Ref. W. It may be explained due to the higher content of portlandite, that provides a chemical buffer, delaying the transformation of C–S–H into M–S–H. Additionally, the formation of expansive sulfate phases such as gypsum, thaumasite and ettringite can retain physically bound water that also dehydrates within this temperature range (80–200 °C), thereby amplifying the apparent peak intensity [92].

Subsequently, a second DTG peak (labelled b) emerges between 100 and 150 °C is visible, and more pronounced in Ref. Mg than in 15% CS Mg. As reported by Lee et al. [93], this region reflects the overlapping dehydration of sulphate phases, including ettringite, thaumasite, and gypsum. The stronger intensity in Ref. Mg suggests a greater formation of gypsum, due to the higher availability of Ca^{2+} from portlandite. Conversely, the lower intensity in 15% CS Mg supports the hypothesis that less gypsum precipitates and that the dominant degradation product in 15% CS Mg is M–S–H, consistent with a more advanced attack on the C–S–H structure.

Following the sulfate-related dehydration peak between 100 and 145 °C, a third peak (labelled c) emerges between 300 and 410 °C, which is attributed to the dihydroxylation of brucite ($Mg(OH)_2$) and early stages of M–S–H dehydration, mainly due to the dehydroxylation of Si-OH groups in M–S–H, as identified by Lee et al. [93] and Sreenivasan et al. [94]. Both Ref. Mg and 15% CS Mg exhibit noticeable intensities in this region, confirming that magnesium ingress has resulted in the formation of brucite, a typical reaction product of $Ca(OH)_2$ with Mg^{2+}. Because 15% CS Mg contains less portlandite, it likely precipitates less brucite but more M–S–H, indicating that Mg^{2+} ions in that system are more directly involved in the decalcification of C–S–H [95].

The subsequent peak (labelled d), located around 450–520 °C, is commonly associated with the dihydroxylation of portlandite [90], in this region 15% CS Mg shows greater intensity than Ref. Mg. It can be explained considering the overlapping thermal effects of M–S–H. As reported by Bernard et al. [91], water loss at 390–500 °C may also result from dihydroxylation of Si-OH and Mg-OH groups in M–S–H, since its non-crystalline structure and gradual water release [91,94]. Given the assumption that 15% CS Mg has experienced more extensive C–S–H decalcification and likely formed more M–S–H, it is reasonable to attribute the increased intensity at this temperature to the combined contributions of residual portlandite and the dehydroxylation of Mg-OH groups in M–S–H [91].

Finally, the last peak (labelled e), between 600 and 800 °C, attributed to the decomposition of calcium carbonate ($CaCO_3$), is associated with the carbonation of both Ref. Mg and 15% CS Mg, during the sample preparation.

Compared to 180-day results, as shown in Figure 12a,b, Ref. W and 15% CS W mixtures exhibit a greater total mass loss, indicating ongoing hydration. Moreover, no significant differences are observed between Ref. W and 15% CS W, confirming the sustained pozzolanic contribution of CS at extended curing times.

In the TG curve, Figure 12a, the total mass loss between 50 and 1000 °C reaches approximately 24.5% for Ref. W and 23.12% for 15% CS W, thus maintaining the reduced gap previously observed at 180 days. In the first and second peak observed in the 80–200 °C region, that corresponds to the dehydration of C-(A)-S-H gel and AFt/AFm phases [90], the mass loss values are approximately 10.92% for Ref. W and 10.80% for 15% CS W, showing a continued comparable degree of hydration in the 15% CS W and Ref. W. In the second peak located between 400 and 500 °C, which is associated with the dihydroxylation of

portlandite ($Ca(OH)_2$), portlandite content is 22.33% lower for 15% CS W compared to Ref. W due to its partial consumption by the CS. Similar to the obtained by Silva et al. [41] in their previous work. Finally, the peak between 600 and 800 °C associated with the decomposition of calcium carbonate ($CaCO_3$) [88] is equivalent for both samples, likely resulting from carbonation during sample preparation.

However, under $MgSO_4$ exposure, as observed at 180 days, a clear difference persists between Ref. Mg and 15% CS Mg. The intensity of the peak (a) within the 50–100 °C region is slightly higher for Ref. Mg, which can be attributed to the presence of physically absorbed water within the matrix. It can be particularly from hydration products that can retain moisture in the pore structure. Among them, sulfate-containing phases such as gypsum form expansive crystals within pores and strongly retain physically bound water [96].

The intensity of the C–S–H-associated peak (labelled b) in the 15% CS Mg sample is higher than that in 15% CS W. This can be attributed to the formation of expansive sulfate phases, such as gypsum, thaumasite, and ettringite, which are known to precipitate within the pore structure during sulfate attack. These phases can retain significant amounts of physically absorbed water, which evaporates within this temperature range (typically 80–180 °C) and contributes to the apparent increase in DTG peak intensity. This behavior aligns with observations reported in previous works [92]. However, the Ref. Mg sample exhibits an even higher peak intensity in this region, indicating a greater accumulation of sulfate phases capable of retaining physically absorbed water. This is likely due to the higher availability of $Ca(OH)_2$ in the reference mix, which enhances the precipitation of gypsum and other sulfate compounds. Consequently, the larger quantity of physically absorbed water released in this temperature range further intensifies the DTG signal in Ref. Mg compared to 15% CS Mg.

Subsequently, the third peak (labelled c) between 100 and 150 °C is more pronounced in Ref. Mg than in 15% CS Mg. As reported by Lee et al. [93], and discussed above, this region reflects the overlapping dehydration of sulphate phases, and then the stronger intensity in Ref. Mg suggests a greater formation of gypsum, compared to 15% CS.

A fourth peak (labelled d) observed between 300 and 410 °C is attributed to the dihydroxylation of brucite ($Mg(OH)_2$) and early stages of M–S–H dehydration, as identified by Lee et al. [93] and Sreenivasan et al. [94], and explained before. Both Ref. Mg and 15% CS Mg exhibit noticeable intensities in this region, confirming the presence of brucite and M–S–H.

The subsequent peak (labeled e), located between 450 and 520 °C, commonly associated with the dihydroxylation of portlandite ($Ca(OH)_2$) [70], displays greater intensity for Ref. Mg compared to 15% CS Mg. While this can be partly attributed to the initially higher $Ca(OH)_2$ content in the reference mix, the contribution of overlapping thermal effects from M–S–H phases must also be considered. As reported by Bernard et al. [91] and discussed previously, water loss in the 390–500 °C range may also result from the dehydroxylation of Si–OH and Mg–OH groups in M–S–H, especially in systems with high Mg/Si ratios [91,92,94]. At 360 days, the higher intensity in Ref. Mg may suggest that the decalcification of C–S–H has initiated, leading to the formation of M–S–H alongside residual portlandite. This behavior contrasts with the situation at 180 days, where Ref. Mg still maintained a buffered system dominated by $Ca(OH)_2$.

Finally, the last peak, between 600 and 800 °C, attributed to the decomposition of calcium carbonate ($CaCO_3$), is associated with the carbonation of both Ref. Mg and 15% CS Mg, during the sample preparation.

3.4.3. FTIR Analyses

Figure 13 exhibits the FTIR spectra of OPC pastes and those incorporating 15 vol% of CS as cement replacement after 28 days of water curing, while Figure 14 shows the corresponding spectra after 180 days of exposure to either water or a 5% $MgSO_4$ solution.

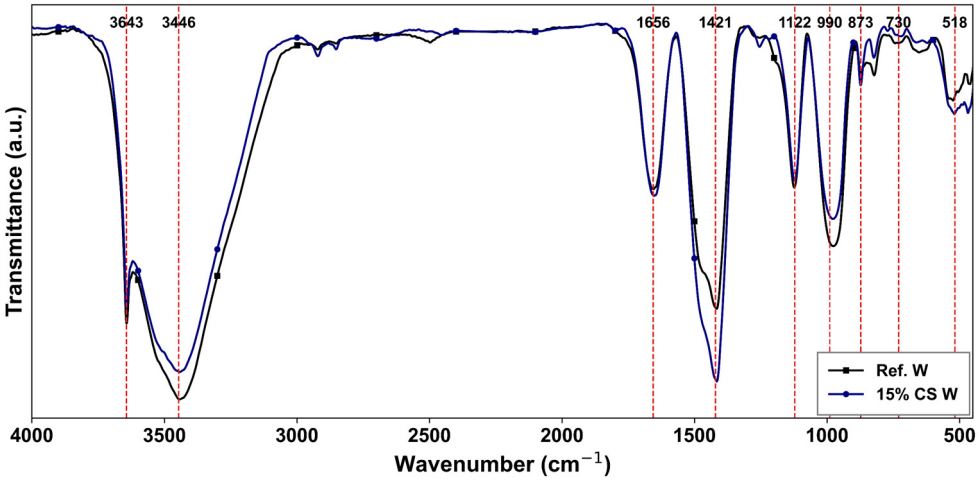

Figure 13. FTIR results at the age of 28 days for the studied cement pastes (red dashed lines indicate main vibrational bands).

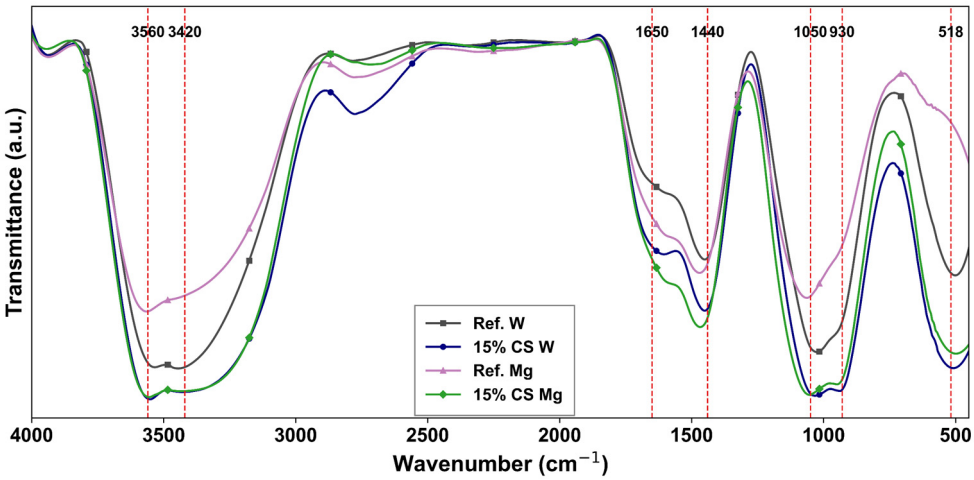

Figure 14. FTIR results at the age of 180 days for the studied cement pastes exposed to magnesium sulphate (red dashed lines indicate main vibrational bands).

In both Figures 13 and 14, the broad band between 3643 and 3446 cm^{-1} region corresponds to the O-H stretching vibrations, related to chemically bound water in calcium hydroxide (portlandite) and C–S–H phases, as previously reported by Silva et al. [90] in their study. At 28 days (Figure 13), the intensity of this band is slightly lower for the 15% CS W, likely due to the dilution effect associated with clinker replacement, which delays hydration reactions in early stages, as it has also been confirmed by Mahajan et al. [40]. In the same period, the band at 1656 cm^{-1}, linked to H-O-H bending from absorbed water or hydration products shows a slightly higher intensity in Ref. W, which suggests a higher degree of hydration at this stage. The shoulder at 1421 cm^{-1} and the region between 873 and 730 cm^{-1} are associated with the stretching vibrations of CO_3^{2-} groups, resulting from carbonation reactions of $Ca(OH)_2$ or unreacted Clinker particles, with atmospheric CO_2, probably during the sample preparation. The 15% CS W sample exhibits slightly higher intensities at 1421 and 873 cm^{-1}, possibly due to the greater exposure of unreacted clinker

particles to atmospheric CO_2 at early ages. The peaks near 1122 cm^{-1}–990 cm^{-1}, and 518 cm^{-1}, are related to asymmetric stretching vibrations of Si-O-Si and Si-O-Al present in the C–S–H gel, as reported by [90]. Both Ref. W and 15% CS W show a similar and slightly higher intensity signal, respectively, in these regions, suggesting that the 15% CS replacement is able to compensate the cement reduction through a filler effect, as reported by [89], promoting C–S–H formation.

After 180 days of water curing (Figure 14), the intensity of the O-H band (region 3560–3435 cm^{-1}) is notably higher in 15% CS W compared to Ref. W. This enhancement is attributed to pozzolanic reactions between CS and portlandite at later ages, generating additional C–S–H and increasing the overall degree of hydration, as confirmed by Silva et al. [28]. Likewise, the H–O–H bending vibration band (around 1650 cm^{-1}) is noticeably higher in the 15% CS W sample compared to Ref. W. This increased intensity may be attributed to the greater amount of C–S–H formed at later ages, which is indicative of a higher degree of hydration [28]. Consequently, this leads to a greater amount of chemically bound water in the matrix, explaining the higher absorbance observed in this region.

Consequently, the asymmetric stretching band of CO_3^{2-} (around 1440 cm^{-1}) is associated with carbonates formation [90]. After 180 days of water curing, 15% CS W shows a slightly higher intensity than Ref. W, which may be attributed to early carbonation during sample preparation and the finer pore structure generated by the addition of CS. After $MgSO_4$ exposure, both samples show comparable trends, suggesting that carbonation proceeds proportionally across all systems, possibly coexisting with sulfate-induced transformations. Additionally, the bands observed near 1050 and 930 cm^{-1} are associated with the asymmetric stretching of Si–O–Si and Si–O–Al bonds, characteristic of C–S–H gel [90]. After 180 days of water curing, 15% CS W shows broader and more intense peaks in this region, indicating the formation of additional C–S–H due to pozzolanic reactions [28]. A similar pattern is observed at 518 cm^{-1}, suggesting a more developed silicate network and possible contributions from hydrated aluminates.

Following $MgSO_4$ exposure (Figure 14), the O-H band intensity within the same region significantly decreases in Ref. Mg, while for 15% CS Mg, a significant change is not observed. This reduction for Ref. Mg reflects the consumption of $Ca(OH)_2$ due to brucite formation ($Mg(OH)_2$), as a result of magnesium sulfate attack (see Equation (1)), according to the report by Bonen et al. [97], as well as a reduction in the chemically bound water in C–S–H, due to the destabilization of C–S–H gel due to sulfate salt that reacts with the C–S–H phase, leading to loss of calcium that may transform into the magnesium silicate hydrate (M–S–H) phase [97,98].

$$MgSO_4 + Ca(OH)_2 \rightarrow Mg(OH)_2 \text{ (brucite)} + CaSO_4 \text{ (gypsum)} \quad (1)$$

For 15% CS Mg, which does not exhibit a significant difference in the O–H stretching region compared to its counterpart, this behavior can be attributed to a reduced availability of $Ca(OH)_2$ resulting from both the lower clinker content and the pozzolanic reactions of CS at later ages [28]. Consequently, the potential for brucite formation is already limited due to the prior consumption of $Ca(OH)_2$, as previously demonstrated in studies involving slag (40% vol.) [99] and silica fume (6% vol.) [100], both of which were successfully incorporated to enhance sulfate resistance. Nonetheless, magnesium ions can still destabilize the C–S–H, converting it into M–S–H, a fibrous and non-cementitious product, which may also contribute to chemically bound water, and has been particularly observed in cementitious systems that contain SCMs, such us blast furnace slag [101] and silica fume [95].

It is important to note that while M–S–H does not contribute appreciably to the early mass loss observed in TGA (80–200 °C), it can nevertheless influence the O–H stretching region in FTIR due to the presence of chemically bound hydroxyl groups. Therefore,

the absence of a clear reduction in this band (region 3560–3435 cm^{-1}) for 15% CS Mg does not contradict the TG/DTG findings.

Subsequently, the intensity of the H–O–H bending vibration band (around 1650 cm^{-1}) is noticeably higher for 15% CS than for Ref. Mg. While this increase could be attributed to greater gypsum formation, such an explanation is less likely in this case due to the reduced availability of Ca^{2+} in CS-blended cements. As it was prior mentioned, the incorporation of CS lowers $Ca(OH)_2$ content through pozzolanic reactions, thereby limiting the formation of brucite and gypsum [95]. Instead, the higher intensity observed in this region can be more feasible associated with increased water retention linked to the formation of M–S–H phases [102]. Thus, beyond reducing the generation of expansive degradation products, the presence of CS appears to modify the nature of the hydration products in a way that promotes higher physically and chemically bound water retention, as it was shown for the M–S–H assessed in this study [103].

In the case of the Si–O stretching band (~930–950 cm^{-1}) all samples exhibit peak broadening and slight intensity loss, especially in Ref. Mg. This broadening reflects progressive loss of silicate chain order consistent with decalcification of C–S–H and its transformation into more disordered M–S–H. Similar spectral changes have been reported by Jin et al. [103], who observed peak broadening in FTIR spectra of C–S–H subjected to leaching in NH_4Cl, attributed to silicate chain cross-linking and structural degradation. This effect is less pronounced in 15% CS Mg, supporting the idea that CS mitigates deterioration by promoting denser C–S–H or the formation of more chemically stable M–S–H non-cementitious gels. Interestingly, the consistently higher intensity at ~518 cm^{-1} in 15% CS Mg, suggests that SCM incorporation may favor the presence of aluminum within the magnesium silicate phases forming magnesium (alumino) silicate hydrates (M-(A)-S-H) [102]. Although M–(A)–S–H phases are reported in the literature for systems containing reactive Al sources, our data did not provide direct spectral evidence of aluminum incorporation. Therefore, the presence of M–S–H is confirmed, but the formation of M–(A)–S–H remains speculative in this study.

Overall, incorporating 15 vol% of CS partially enhances the sulfate resistance of cement pastes by reducing the formation of brucite and gypsum, preserving the C–S–H gel, and possibly promoting the development of M–S–H or M–A–S–H phases. Although these magnesium-based phases are not cementitious [94], they are considerably less expansive and deleterious than gypsum, thereby contributing to reduced deterioration [91]. Moreover, the presence of CS supports greater bound water retention and improved structural stability under aggressive $MgSO_4$ exposure.

3.4.4. SEM Analysis

Microstructural characterization by SEM was performed on both matrices (100% OPC and 85% OPC–15% CS) after curing in water and after exposure to the $MgSO_4$ solution. Figure 15 shows the SEM images of the matrices at 180 days. It can be observed that the mixtures cured in water exhibit a homogeneous structure. However, for the mixtures exposed to the $MgSO_4$ solution, the matrix with 100% OPC shows microcracks (highlighted in yellow boxes), which may be attributed to the accumulation of expansive products. In the image taken at 8000× magnification for the OPC sample, the formation of ettringite (AFt) is observed, although in smaller amounts compared to the Na_2SO_4 attack. This difference is consistent with the specific mechanism of $MgSO_4$ attack, in which it reacts with portlandite and C–S–H gel to form $Mg(OH)_2$ (brucite) and gypsum ($CaSO_4 \cdot 2H_2O$), with minimal AFt production. In the image corresponding to the 15% CS matrix, slatted ettringite can be observed. Its morphology varies due to the pH of the mixture, which influences the shape and formation of the crystals [104].

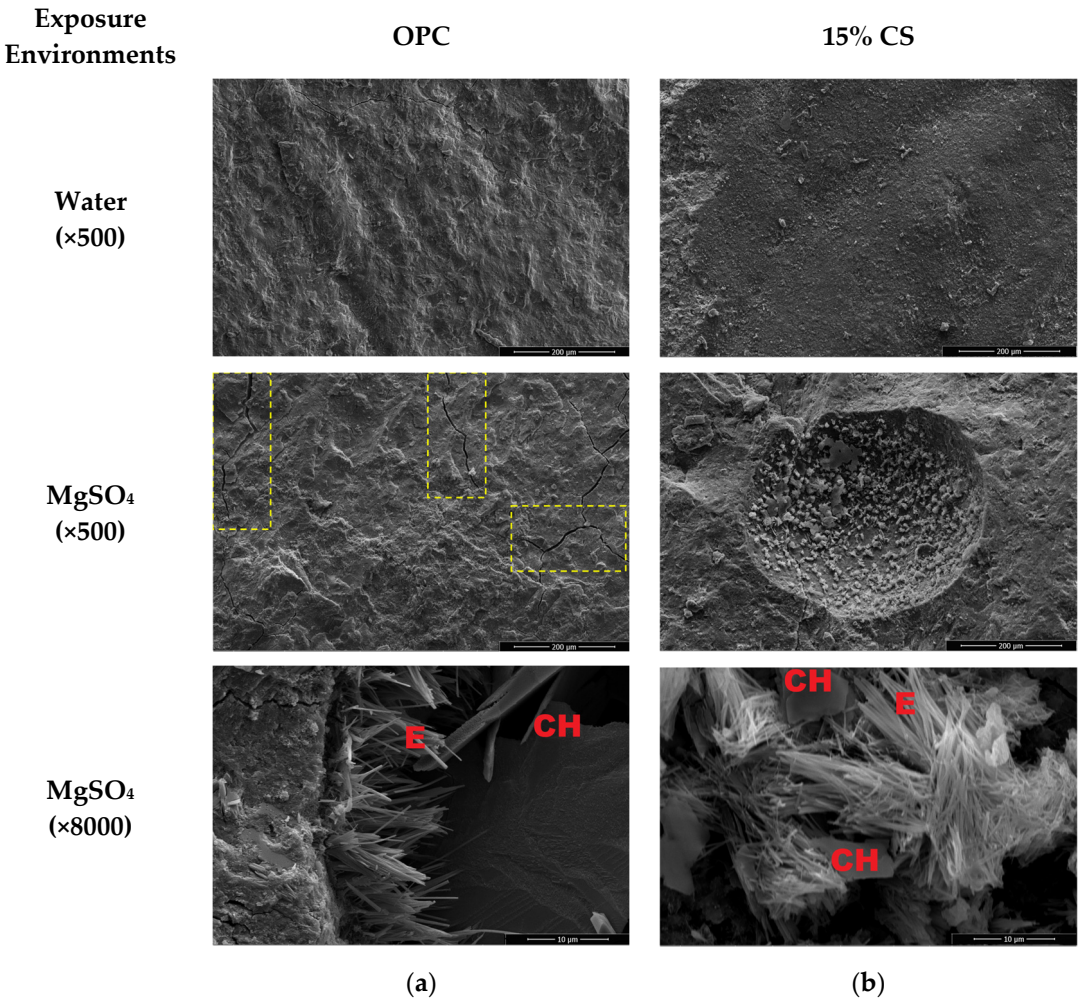

Figure 15. SEM of cement paste mixtures exposed to water and (**a**) OPC (100% OPC) mixture; (**b**) 15% CS (85% OPC and 15% CS).

Although the transformation from C–S–H to M–S–H is inferred through converging evidence from FTIR and TGA, future work should include SEM–EDS or STEM–EDS mapping to directly confirm spatial gradients in decalcification and Mg uptake.

While the present study evaluated magnesium sulfate attack through visual inspection, porosity, density, and strength loss, it did not include direct quantification of Mg^{2+} or $SO_4{}^{2-}$ ingress. Such measurements, whether via chemical profiling or modeling, could offer deeper insight into ion transport mechanisms and degradation front evolution. Future work should incorporate approaches such as those described by Ding et al. [105] where advection–diffusion transport equations with time- and space-dependent boundary conditions are applied to simulate aggressive ion penetration in cementitious matrices.

In summary, the results of this study demonstrate the potential of copper slag (CS) to mitigate sulfate-induced deterioration mechanisms, primarily by reducing portlandite content and promoting the formation of less expansive M–S–H phases. However, alternative SCM systems—such as ground granulated blast furnace slag, metakaolin, and alkali-activated binders—have shown strong sulfate resistance under similar exposure conditions, due to their refined pore structures and reduced CH content (e.g., [106–108]). While the present study focuses on CS due to its local abundance and dual functionality, future work should include head-to-head comparisons with these systems to assess performance and scalability under aggressive environments, such as $MgSO_4$ exposure. In this regard, Luo et al. [109] recently demonstrated that optimizing the CaO/Al_2O_3 and

SiO_2/Al_2O_3 molar ratios in slag/fly ash-based geopolymers can significantly improve the mechanical performance and water stability of stabilized clays. Their findings reveal that the balance between geopolymerization and hydration reactions plays a critical role in durability performance, offering valuable insight for future comparative studies involving SCM-based systems exposed to sulfate-rich environments.

4. Conclusions

This study evaluated the performance of concrete mixtures containing a 15 vol% partial replacement of ordinary Portland cement (OPC) with copper slag (CS) as supplementary cementitious material (SCM), along with 0%, 20%, 50%, and 100% replacement of natural coarse aggregate by recycled coarse aggregate (RCA) sourced from construction and demolition concrete waste. Replacing 15% of cement with CS, a non-carbon-emitting byproduct, is estimated to reduce binder-related CO_2 emissions by approximately 5.7% [4]. Similarly, RCA use avoids primary aggregate extraction and landfill disposal, advancing circular material flows in construction. The mixtures were evaluated based on their compressive strength under water curing conditions and exposure to a 5% $MgSO_4$ solution, as well as through structural analysis. The main findings of this study are outlined below:

1. The visual degradation of the mixtures intensifies as the exposure period extended from 180 to 360 days, with more pronounced deterioration observed along specimen edges. Additionally, the white layer on the surface became more clearly defined and exhibited some cracking, indicating a more severe sulfate attack over time. However, no significant visual differences were observed between the mixture M2 (15% CS and 0% RCA) and those containing increasing dosages of RCA (M3, M4, and M5, with 20%, 50%, and 100% of RCA, respectively).
2. The incorporation of 15% CS as SCM for OPC reduced compressive strength at early ages (e.g., 28 and 56 days). However, this effect diminishes over time, and at later curing ages (e.g., 388 days), the strength becomes comparable to that of the reference mixture. Conversely, the use of recycled concrete aggregate (RCA) results in a monotonic decrease in compressive strength as the RCA content increases, regardless of the curing age.
3. At 28 and 100 days of exposure, an increase in compressive strength was observed in cementitious mixtures, whether or not they contained CS and/or RCA, when added to a 5% $MgSO_4$ solution. This short-term gain is attributed to pore filling by expansive phases such as gypsum and ettringite. However, at longer exposure durations (180 and 360 days), all mixtures showed a loss in mechanical strength. This long-term loss is associated with the progressive degradation of the binding matrix, including C–S–H decalcification, M–S–H formation, and internal cracking.
4. Fourier-transform infrared spectroscopy (FTIR) analyses revealed that the presence of 15% CS modifies the sulfate magnesium attack mechanism by partially converting C–S–H into M–S–H. Compared to the Ref., the CS-blended paste exhibited reduced formation of brucite and gypsum, indicating a less expansive and less damaging degradation mechanism. This behavior suggests that CS contributes to stabilizing the microstructure under $MgSO_4$ exposure by promoting the formation of more stable, but non-cementitious hydrates.
5. TGA/DTG results demonstrate that incorporating 15 vol% CS modifies the thermogravimetric performance of the cement paste under $MgSO_4$ exposure. The intensity reduction of the C–S–H peak and the distinct peak intensity between 390 and 500 °C suggests the formation of M–S–H resulting from magnesium-induced decalcification. Compared to the Ref., CS-blended cement exhibited lower brucite and gypsum-related mass losses, indicating a less aggressive degradation process. Additionally, the re-

duced portlandite content in CS-blended cement samples reflect the simultaneous effect of pozzolanic reaction and sulfate attack, highlighting a degradation mechanism distinct from pure OPC.

As a future study, higher CS dosages and hybrid SCMs should be tested for optimal strength/densification, as well as examining the impact of using RCA surface pretreatments—such as surface treatments, pozzolanic coatings, or pre-saturation techniques—and using optimized mixing protocols that employ stabilizers, water-reducing admixtures, or graded RCA blending. Finally, a cradle-to-gate life cycle assessment (LCA) is recommended.

Author Contributions: Methodology, Y.F.S., C.B. and G.A.-L.; Validation, Y.F.S., A.R.-R. and G.A.-L.; Formal analysis, Y.F.S., C.B., E.J.R. and G.A.-L.; Investigation, Y.F.S., C.B., E.J.R. and G.A.-L.; Resources, Y.F.S.; Data curation, Y.F.S.; Writing—original draft, Y.F.S., C.B., E.J.R., A.R.-R. and G.A.-L.; Writing—review and editing, Y.F.S., C.B. and G.A.-L.; Visualization, Y.F.S. and G.A.-L.; Supervision, Y.F.S. and G.A.-L.; Project administration, Y.F.S.; Funding acquisition, Y.F.S. All authors have read and agreed to the published version of the manuscript.

Funding: This work was financially supported by the National Agency for Research and Development (ANID) through Fondecyt Regular Project No. 1250096, the Scholarship ANID Doctorado Nacional 2022 Folio 21221769 and Academic Insertion Program (PIA-UC). The authors would also like to thank the Concrete Innovation Center (CIH-UC), Coldelco, Sika and Sergio Valenzuela for his valuable assistance with the concrete mixing process and the evaluation of mechanical properties.

Institutional Review Board Statement: Not applicable.

Informed Consent Statement: Not applicable.

Data Availability Statement: The original contributions presented in this study are included in the article. Further inquiries can be directed to the corresponding authors.

Conflicts of Interest: The authors declare no conflict of interest.

Abbreviation

Abbreviation	Full Term/Description
AFt	Alumina-ferrite trisulfate (ettringite) phase
ASTM	American Society for Testing and Materials
C–S–H	Calcium-silicate hydrate
CDW	Construction-and-demolition waste
CH	Portlandite, $Ca(OH)_2$
CS	Copper slag (supplementary cementitious material)
DTG	Differential thermogravimetric curve
FTIR	Fourier-transform infrared spectroscopy
ESA	External sulfate attack
ITZ	Interfacial transition zone
$MgSO_4$	Magnesium sulfate
M–S–H	Magnesium-silicate hydrate
NA	Natural aggregate
NCA	Natural coarse aggregate
NFA	Natural fine aggregate
OPC	Ordinary Portland cement
RCA	Recycled coarse aggregate
SCM	Supplementary cementitious material
SEM	Scanning electron microscopy
SEM-EDS	SEM coupled with energy-dispersive X-ray spectroscopy
SP	Superplasticizer (high-range water-reducing admixture)

TG/TGA	Thermogravimetric analysis
w/c	Water-to-cement ratio
XRD	X-ray diffraction

References

1. Ma, X.; Hu, H.; Luo, Y.; Yao, W.; Wei, Y.; She, A. A Carbon Footprint Assessment for Usage of Recycled Aggregate and Supplementary Cementitious Materials for Sustainable Concrete: A Life-Cycle Perspective in China. *J. Clean. Prod.* **2025**, *490*, 144772. [CrossRef]
2. Kanagaraj, B.; Anand, N.; Lubloy, E. Sustainability and Durability Performance Evaluation of Geopolymer Concrete with Industrial Effluent as Alternative to Conventional River Sand. *Dev. Built Environ.* **2024**, *19*, 100517. [CrossRef]
3. Rosales, J.; Rosales, M.; Cabrera, M.; Cubero, A.; Agrela, F.; Redel, M.D. Biomass Bottom Ash in Different Types of Recycled Concrete. Mechanical, Acoustic and Thermal Properties. *J. Build. Eng.* **2025**, *107*, 112724. [CrossRef]
4. Arredondo, P.W.C.; Silva, Y.F.; Araya-Letelier, G.; Hernández, H. Valorization of Recycled Aggregate and Copper Slag for Sustainable Concrete Mixtures: Mechanical, Physical, and Environmental Performance. *Sustainability* **2024**, *16*, 11239. [CrossRef]
5. Lliso-Ferrando, J.R.; Arenós-Barrachina, A.; Monzón-Bello, P.; Valcuende, M. Durability of Mortars with Par-tial Cement Replacement by Recycled Brick Powder. *Appl. Sci.* **2025**, *15*, 4133. [CrossRef]
6. Sbahieh, S.; McKay, G.; Nurdiawati, A.; Al-Ghamdi, S.G. The Sustainability of Partial and Total Replacement of Ordinary Portland Cement: A Deep Dive into Different Concrete Mixtures through Life Cycle Assessment. *J. Build. Eng.* **2025**, *108*, 112830. [CrossRef]
7. Kaminskas, R.; Barauskas, I.; Uselis, S.; Savickaite, B. Binary Supplementary Cementitious Material from Ex-panded Clay Production Dust and Opoka. *Sustainability* **2025**, *17*, 794. [CrossRef]
8. Navaneetha, E.; Rao, P.N.; Bahurudeen, A. Development of Sustainable and Durable Ternary Blended Con-crete Using Sugarcane Bagasse Ash and Glass Powder. *Constr. Build. Mater.* **2025**, *466*, 140329. [CrossRef]
9. Chen, L.; Huang, Z.; Pan, W.; Su, R.K.L.; Zhong, Y.; Zhang, Y. Low Carbon Concrete for Prefabricated Modu-lar Construction in Circular Economy: An Integrated Approach towards Sustainability, Durability, Cost, and Mechanical Performances. *J. Build. Eng.* **2024**, *90*, 109368. [CrossRef]
10. Kaptan, K.; Cunha, S.; Aguiar, J. A Review of the Utilization of Recycled Powder from Concrete Waste as a Cement Partial Replacement in Cement-Based Materials: Fundamental Properties and Activation Methods. *Appl. Sci.* **2024**, *14*, 9775. [CrossRef]
11. Silva, Y.F.; Izquierdo, S.; Delvasto, S.; Araya-Letelier, G. Carbonation and Chloride Penetration Performance of Self-Compacting Concrete with Masonry and Concrete Wastes. *Eur. J. Environ. Civ. Eng.* **2024**, *29*, 744–758. [CrossRef]
12. Silva, Y.F.; Delvasto, S.; Izquierdo, S.; Araya-Letelier, G. Short and Long-Term Physical and Mechanical Characterization of Self-Compacting Concrete Made with Masonry and Concrete Residue. *Constr. Build. Mater.* **2021**, *312*, 125382. [CrossRef]
13. Temelli, U.E.; Sezgin, N.; Ozdogan Cumali, B.; Nemlioglu, S. Analysis of Construction and Demolition Waste Prediction Post-Earthquake Disasters. *Eng. Sci. Technol. Int. J.* **2025**, *67*, 102078. [CrossRef]
14. Alsheyab, M.A.T. Recycling of Construction and Demolition Waste and Its Impact on Climate Change and Sustainable Development. *Int. J. Environ. Sci. Technol.* **2022**, *19*, 2129–2138. [CrossRef]
15. Bavithra, K.; Mohana, R. Sustainable Development of Durable and Novel Nano GGBS Impregnated Eco-Friendly Green Concrete Using Micro Structural Characterization and Techno-Economic Sustainability Analysis. *Constr. Build. Mater.* **2025**, *470*, 140565. [CrossRef]
16. Kanagaraj, B.; Anand, N.; Samuvel Raj, R.; Lubloy, E. Evaluation of Mechanical, Durability and Sustainability Performance of Geopolymer Concrete Using Sodium Silicate Waste as Source Material. *Case Stud. Constr. Mater.* **2024**, *21*, e03898. [CrossRef]
17. Abushama, W.J.; Tamimi, A.K.; Tabsh, S.W.; El-Emam, M.M.; Ibrahim, A.; Mohammed Ali, T.K. Influence of Optimum Particle Packing on the Macro and Micro Properties of Sustainable Concrete. *Sustainability* **2023**, *15*, 14331. [CrossRef]
18. Shanks, B.; Howe, C.; Draper, S.; Wong, H.; Cheeseman, C. Production of Low-Carbon Amorphous SiO2 for Use as a Supplementary Cementitious Material and Nesquehonite from Olivine. *Mater. Lett.* **2024**, *361*, 136133. [CrossRef]
19. Krishnan, A.; Subramanian, S.S. Effect of Green Gram Pod Ash (GGPA) as Supplementary Cementitious Material (SCM) in Mechanical and Durability Properties of Concrete. *Constr. Build. Mater.* **2024**, *411*, 134663. [CrossRef]
20. Kasaniya, M.; Thomas, M.D.A. Role of the Alkalis of Supplementary Cementing Materials in Controlling Pore Solution Chemistry and Alkali-Silica Reaction. *Cem. Concr. Res.* **2022**, *162*, 107007. [CrossRef]
21. Ishaq, M.B.; Mohammed, A.S.; Mohammed, A.A. The Role of Waste Glass Powder in Alkali-Silica Reaction Mitigation: Transforming Glasscrete Durability through Chemical Composition Dynamics. *Sustain. Chem. Pharm.* **2025**, *45*, 102019. [CrossRef]
22. Mohanty, S.; Sahoo, K.; Samal, K. Progress in Sustainable Vegetation Eco-Concrete Technology: A Review on Materials, Applications and Challenges. *J. Build. Eng.* **2025**, *104*, 112354. [CrossRef]
23. Kumar, P.; Pasla, D.; Thiyagarajan, J.S. Synergetic Effect of Coarse Sintered Fly Ash Aggregates and Supple-mentary Cementitious Materials in Self-Compacting Concrete: From Durability and Corrosion Perspective. *J. Build. Eng.* **2025**, *108*, 112969. [CrossRef]

24. Ouldkhaoua, Y.; Benabed, B.; Abousnina, R.; Kadri, E.H.; Khatib, J. Effect of Using Metakaolin as Supplemen-tary Cementitious Material and Recycled CRT Funnel Glass as Fine Aggregate on the Durability of Green Self-Compacting Concrete. *Constr. Build. Mater.* **2020**, *235*, 117802. [CrossRef]
25. Xiao, R.; Prentice, D.; Collin, M.; Balonis, M.; La Plante, E.; Torabzadegan, M.; Gadt, T.; Sant, G. Calcium Ni-trate Effectively Mitigates Alkali–Silica Reaction by Surface Passivation of Reactive Aggregates. *J. Am. Ceram. Soc.* **2024**, *107*, 7513–7527. [CrossRef]
26. Nieświec, M.; Niewiadomski, P.; Sadowski, Ł.; Schroefl, C. Waste Copper Slag in Special Concrete: Current Research and Future Applications. *Mater. Des.* **2025**, *253*, 113970. [CrossRef]
27. Deep, A.; Zade, N.P.; Sarkar, P. Exploring the Viability of Copper Slag Geopolymer Concrete in Structural Applications: A Study on Strength Variability and Seismic Risk Assessment. *Structures* **2024**, *70*, 107670. [CrossRef]
28. Silva, Y.F.; Burbano-Garcia, C.; Araya-Letelier, G.; González, M. Short- and Long-Term Experimental Per-formance of Concrete with Copper Slag: Mechanical and Physical Properties Assessment. *Case Stud. Constr. Mater.* **2024**, *20*, e03302. [CrossRef]
29. Silva, Y.F.; Villaquirán-Caicedo, M.; Izquierdo, S. Exploring the Potential of Alternative Materials in Con-crete Mixtures: Effect of Copper Slag on Mechanical Properties and Carbonation Resistance. *Materials* **2023**, *16*, 6677. [CrossRef] [PubMed]
30. Moodi, Y.; Hamzehkolaei, N.S.; Afshoon, I. Machine Learning Models for Predicting Compressive Strength of Eco-Friendly Concrete with Copper Slag Aggregates. *Mater. Today Commun.* **2025**, *46*, 112572. [CrossRef]
31. Sahu, A.; Kumar, S.; Srivastava, A.K.L.; Pratap, B. Performance of Recycled Aggregate Concrete Using Cop-per Slag as Fine Aggregate. *J. Build. Eng.* **2024**, *82*, 108364. [CrossRef]
32. Ameri, F.; Shoaei, P.; Zahedi, M.; Karimzadeh, M.; Musaeei, H.R.; Cheah, C.B. Physico-Mechanical Properties and Micromor-phology of AAS Mortars Containing Copper Slag as Fine Aggregate at Elevated Temperature. *J. Build. Eng.* **2021**, *39*, 102289. [CrossRef]
33. Pushpakumara, B.H.J.; Bandara, P.M.K.N. Evaluating the Effectiveness of Copper Slag Waste as a Fine Ag-gregate in Concrete. *Constr. Build. Mater.* **2025**, *475*, 141046. [CrossRef]
34. Ambily, P.S.; Kaliyavaradhan, S.K.; Sebastian, S.; Shekar, D. Sustainable 3D Printable Concrete Mix Using Copper Slag. *J. Build. Eng.* **2025**, *101*, 111950. [CrossRef]
35. Sharifi, Y.; Afshoon, I.; Asad-Abadi, S.; Aslani, F. Environmental Protection by Using Waste Copper Slag as a Coarse Aggregate in Self-Compacting Concrete. *J. Environ. Manag.* **2020**, *271*, 111013. [CrossRef]
36. Lori, A.R.; Hassani, A.; Sedghi, R. Investigating the Mechanical and Hydraulic Characteristics of Pervious Concrete Containing Copper Slag as Coarse Aggregate. Constr. *Build. Mater.* **2019**, *197*, 130–142. [CrossRef]
37. Yadav, A.; Jayappa, S.M.; Mahadevaiah, R.R.; Gowda, S.; Jitesh, N.; Pasmanabh, J.; Anand, V.; Nagarajaiah, M. Exploring the Potential of Copper Slag and Quartz as Fine Aggregate Replacements in Concrete: A Com-prehensive Study. *Eng. Proc.* **2023**, *59*, 224. [CrossRef]
38. Chaitanya, B.K.; Sivakumar, I.; Madhavi, Y.; Cruze, D.; Venkatesh, C.; Naga Mahesh, Y.; Sri Durga, C.S. Mi-crostructural and Residual Properties of Self-Compacting Concrete Containing Waste Copper Slag as Fine Aggregate Exposed to Ambient and Elevated Temperatures. *Infrastructures* **2024**, *9*, 85. [CrossRef]
39. Afshoon, I.; Sharifi, Y. Use of Copper Slag Microparticles in Self-Consolidating Concrete. *ACI Mater. J.* **2017**, *114*, 691–699. [CrossRef]
40. Mahajan, D.S.; Muhammad, S. Assessment of the Viability of Pozzolanic Activity of Copper Slag for Use as Supplementary Cementitious Material in Ordinary Portland Cement. *J. Build. Eng.* **2024**, *83*, 108375. [CrossRef]
41. Silva, Y.F.; Burbano-Garcia, C.; Araya-Letelier, G.; Izquierdo, S. Sulfate Attack Performance of Concrete Mixtures with Use of Copper Slag as Supplementary Cementitious Material. *Case Stud. Constr. Mater.* **2025**, *22*, e04846. [CrossRef]
42. Yuan, Q.; Zhang, J.; Zhang, S.; Zheng, K.; Chen, L. An Eco-Friendly Solution for Construction and Demolition Waste: Recycled Coarse Aggregate with CO_2 Utilization. *Sci. Total Environ.* **2024**, *950*, 175163. [CrossRef]
43. Xu, F.; Wang, S.; Li, T.; Liu, B.; Zhao, N.; Liu, K. The Mechanical Properties and Resistance against the Cou-pled Deterioration of Sulfate Attack and Freeze-Thaw Cycles of Tailing Recycled Aggregate Concrete. *Constr. Build. Mater.* **2021**, *269*, 121273. [CrossRef]
44. de Andrade Salgado, F.; de Andrade Silva, F. Recycled Aggregates from Construction and Demolition Waste towards an Application on Structural Concrete: A Review. *J. Build. Eng.* **2022**, *52*, 104452. [CrossRef]
45. Tam, V.W.Y.; Soomro, M.; Evangelista, A.C.J. A Review of Recycled Aggregate in Concrete Applications (2000–2017). *Constr. Build. Mater.* **2018**, *172*, 272–292. [CrossRef]
46. Amin, M.; Elsakhawy, Y.; Abu el-hassan, K.; Abdelsalam, B.A. Effects of Pozzolanic Treatment Method of Aggregate on Recycled Aggregate High Strength Concrete Properties. *J. Build. Eng.* **2025**, *108*, 112898. [CrossRef]
47. Jin, L.; Wang, Z.; Wu, T.; Xie, Z.; Xue, P. Damage-Based Ion Transport in Recycled Aggregate Concrete under External Sulfate Attack. *Constr. Build. Mater.* **2024**, *445*, 137944. [CrossRef]
48. Singh, P.K.; Rajhans, P. Experimental Investigation and SVR Model to Predict the Mechanical Properties of RAC by Enhancing the Characteristic of RCA Using Surface Treatment Method along with Modified Mixing Approach. *Constr. Build. Mater.* **2023**, *393*, 132032. [CrossRef]

49. Hou, Y.; Zhang, X.; Liu, J.; He, C.; Ji, X. Interface Adhesion Enhancement and Multi-Scale Evaluation of Recy-cled Concrete Aggregate(RCA) and Asphalt. *Constr. Build. Mater.* **2024**, *457*, 139271. [CrossRef]
50. Jia, Y.; Ding, M.; Lin, Y.; Wang, L.; Wei, Y.; Han, S. Effect of Pozzolanic Slurry Coating Containing Nano-Alumina on Macro-Micro Properties of Recycled Brick Aggregate. *Constr. Build. Mater.* **2025**, *459*, 139752. [CrossRef]
51. Ren, X.; Yang, J.; Chen, W.; Huang, Y.; Wang, G.; Niu, J.; Wu, J. Effect of Recycled Concrete Powder-Cement Composite Coating Modification on the Properties of Recycled Concrete Aggregate and Its Concrete. *Constr. Build. Mater.* **2024**, *444*, 137860. [CrossRef]
52. Allal, M.; Zeghichi, L.; Siline, M. Optimization of the Recycled Aggregate Processing Using the Full Factorial Design Approach, Chemical, Physical and Microstructural Characterization of Treated Aggregates by Pre-Coated with Cementitious Paste. *J. Build. Eng.* **2024**, *94*, 109852. [CrossRef]
53. Zhang, H.; Yi, S.; Xu, X.; Yao, J. New Insights into Impacts of Pre-Wetting Strategies of Recycled Coarse Ag-gregate (RCA) on Microstructure and Performance of Concrete. *J. Build. Eng.* **2025**, *99*, 111525. [CrossRef]
54. Kang, J.; Liang, F.; Yang, J.; Yu, Z.; Chen, X.; Tian, Y. Development of Green and Economical Recycled Aggre-gate Concrete through Mineral Admixtures and Carbonated Recycled Coarse Aggregate. *Mater. Today Commun.* **2025**, *46*, 112531. [CrossRef]
55. Agwa, I.S.; Mostafa, S.A.; Abd-Elrahman, M.H.; Amin, M. Effect of Recycled Aggregate Treatment Using Fly Ash, Palm Leaf Ash, and Silica Fume Slurries on the Mechanical and Transport Properties of High-Strength Concrete. *J. Build. Eng.* **2025**, *111*, 113292. [CrossRef]
56. Qin, S.; Zhang, M.; Zou, D.; Liu, T.; Li, Y. Mesoscale Modeling of Mechanical Deterioration in Sul-fate-Attacked Concrete. *Eng. Fract. Mech.* **2025**, *323*, 111219. [CrossRef]
57. Silva, Y.F.; Delvasto, S. Sulfate Attack Resistance of Self-Compacting Concrete with Residue of Masonry. *Constr. Build. Mater.* **2021**, *268*, 121095. [CrossRef]
58. El Inaty, F.; Aydin, B.; Houhou, M.; Marchetti, M.; Quiertant, M.; Omikrine Metalssi, O. Long-Term Effects of External Sulfate Attack on Low-Carbon Cementitious Materials at Early Age. *Appl. Sci.* **2024**, *14*, 2831. [CrossRef]
59. Lothenbach, B.; Le Saout, G.; Gallucci, E.; Scrivener, K. Influence of Limestone on the Hydration of Portland Cements. *Cem. Concr. Res.* **2008**, *38*, 848–860. [CrossRef]
60. Belghali, M.; Ayed, K.; Ezziane, M.; Leklou, N. The Influence of Sulfate Attack on Existing Concrete Bridges: Study of External Sulfate Attack (ESA). *Constr. Build. Mater.* **2025**, *483*, 141751. [CrossRef]
61. Zhang, L.; Yao, J.; Tong, Y. Eccentric Compression Behavior of Fibers Lithium Slag Concrete Columns Sub-jected to Loading and Sulfate Attack. *KSCE J. Civ. Eng.* **2025**, *29*, 100236. [CrossRef]
62. Wang, J.; Fu, M.; Zheng, K.; Zhang, K.; Fan, Y.; Niu, D. Ion Transport Mechanism and Diffusion Model Estab-lishment in Recycled Aggregate Concrete Subjected to Magnesium, Sulfate, and Chloride Attack. *Constr. Build. Mater.* **2024**, *428*, 136273. [CrossRef]
63. *ASTM C150*; Standard Specification for Portland Cement. ASTM International: West Conshohocken, PA, USA, 2022; pp. 1–9.
64. *ASTM C136/C136M*; Standard Test Method for Sieve Analysis of Fine and Coarse Aggregates. ASTM International: West Conshohocken, PA, USA, 2019; In Proceedings of the Astm C136-14, pp. 1–5.
65. *ASTM C128*; Standard Test Method for Relative Density (Specific Gravity) and Absorption of Fine Aggregate. ASTM International: West Conshohocken, PA, USA, 2022; Volume I, pp. 1–6.
66. *ASTM C127*; Standard Test Method for Relative Density (Specific Gravity) and Absorption of Coarse Aggregate. ASTM International: West Conshohocken, PA, USA, 2024; pp. 1–6.
67. *ASTM C192/C192M-25*; Standard Practice for Making and Curing Concrete Test Specimens in the Laboratory. ASTM International: West Conshohocken, PA, USA, 2025. [CrossRef]
68. *ASTM C39 ASTM C39/39M*; Standard Test Method for Compressive Strength of Cylindrical Concrete Specimens. ASTM International: West Conshohocken, PA, USA, 2018.
69. *ASTM C642 ASTM C642*; Standard Test Method for Density, Absorption, and Voids in Hardened Concrete. ASTM International: West Conshohocken, PA, USA, 2021.
70. Carrasco, M.; Araya-letelier, G.; Velázquez, R.; Visconti, P. Image-based Automated Width Measurement of Surface Cracking. *Sensors* **2021**, *21*, 7534. [CrossRef] [PubMed]
71. Gunjal, S.M.; Turkane, S.D.; Patankar, S.V.; Kondraivendhan, B. Effect of Magnesium Sulphate and Sul-phuric Acid Attack on Limestone Calcined Clay Cement Concrete. *Mater. Today Proc.* 2023, *in press*. [CrossRef]
72. Yan, D.; Chen, S.; Jin, J.; Zhu, X.; Wang, J.; Zeng, Q. Chemical–Physical–Mechanical Stability of MKG Mortars under Sulfate Attacks. *Adv. Cem. Res.* **2021**, *33*, 224–238. [CrossRef]
73. Sun, L.; Lan, S.; Wang, C. Durability and Microstructural Evolution of Seawater Sea-Sand Coral Concrete under Different Exposure Environments of Sulfate Attack. *Constr. Build. Mater.* **2025**, *478*, 141399. [CrossRef]
74. Wang, Y.; Hu, Y.; Yang, J.; He, Y.; He, X.; Su, Y.; Strnadel, B. Performance of Cement-Based Materials Incor-porating Ultra-Fine Copper Slag. *Constr. Build. Mater.* **2023**, *402*, 132949. [CrossRef]

75. Arif, R.; Javed, M.F.; Asghar, R.; Iqtidar, A.; Ahmed, B.; Alyousef, R.; Khan, M.A. A Scientometric Review on the Utilization of Copper Slag as a Substitute Constituent of Ordinary Portland Cement Concrete. *Rev. Adv. Mater. Sci.* **2025**, *64*, 20240082. [CrossRef]
76. Joseph, H.S.; Pachiappan, T.; Avudaiappan, S.; Guindos, P. Prediction of the Mechanical Properties of Con-crete Incorporating Simultaneous Utilization of Fine and Coarse Recycled Aggregate. *Rev. De La Constr.* **2023**, *22*, 178–191. [CrossRef]
77. Xuyong, C.; Jiawei, M.; Qiaoyun, W.; Jie, L.; Shukai, C.; Zhuo, L. Study of the Effect of Pretreatment on Coarse Recycled Aggregate in Self-Compacting Concrete: Rheology, Mechanical Properties, and Microstructures. *J. Build. Eng.* **2025**, *101*, 111744. [CrossRef]
78. Wang, W.; Shen, A.; Zhou, J.; Ebohon, O.J.; Zhan, Q. Combined Influence and Mechanism of Superabsorbent Polymers and Waterborne Epoxy Coatings on the Durability of Self-Curing Concrete under Compound So-dium and Magnesium Sulfate Attacks. *Case Stud. Constr. Mater.* **2025**, *22*, e04585. [CrossRef]
79. Jia, R.; Wang, Q.; Luo, T. Mechanisms and Differences between Sodium and Magnesium Sulfate Attacks on Alkali-Activated Phosphorus Slag. *Constr. Build. Mater.* **2023**, *403*, 133117. [CrossRef]
80. Al-Kerttani, O.M.G.; Hilal, N.; Hama, S.M.; Sor, N.H.; Banyhussan, Q.S.; Tawfik, T.A. Durability and Hard-ened Characteristics of Cement Mortar Incorporating Waste Plastic and Polypropylene Exposed to $MgSO_4$ Attack. *Results Eng.* **2024**, *24*, 103310. [CrossRef]
81. Zhang, H.; Ji, T.; Liu, H. Performance Evolution of Recycled Aggregate Concrete (RAC) Exposed to External Sulfate Attacks under Full-Soaking and Dry-Wet Cycling Conditions. *Constr. Build. Mater.* **2020**, *248*, 118675. [CrossRef]
82. Yu, Z.; Li, Y.; Liu, Y.; Shen, X. Role of Porous Aggregate Types on the Sulfate Attack Resistance of Cement Mortar. *Constr. Build. Mater.* **2025**, *483*, 141781. [CrossRef]
83. Wang, J.; Fan, Y.; Che, Z.; Zhang, K.; Niu, D. Study on the Durability of Eco-Friendly Recycled Aggregate Concrete with Supplementary Cementitious Materials: The Combined Action of Compound Salt Solution of $MgSO_4$, Na_2SO_4, and NaCl and Dry-Wet Cycles. *Constr. Build. Mater.* **2023**, *377*, 131149. [CrossRef]
84. Durgun, M.Y.; Sevinç, A.H. Determination of the Effectiveness of Various Mineral Additives against Sodium and Magnesium Sulfate Attack in Concrete by Taguchi Method. *J. Build. Eng.* **2022**, *57*, 104849. [CrossRef]
85. Burbano-García, C.; Silva, Y.F.; Araya-Letelier, G.; González, M. Hydration Kinetics and Mechanical Performance of Cement Pastes with Copper Slag as Supplementary Cementitious Material. Manuscript under review. *J. Build. Eng.* 2025, *accepted*.
86. Zhu, J.F.; Wang, Z.Q.; Tao, Y.L.; Ju, L.Y.; Yang, H. Macro–Micro Investigation on Stabilization Sludge as Sub-grade Filler by the Ternary Blending of Steel Slag and Fly Ash and Calcium Carbide Residue. *J. Clean. Prod.* **2024**, *447*, 141496. [CrossRef]
87. Hua, T.; Cao, Z.; Zhang, S.; Guo, R. Dual Mechanism of CaO-Based Expansive Agent on Sulfate Attack of Marine Concrete: Competitive Interaction between Pore Structure and Hydration Products. *Constr. Build. Mater.* **2025**, *487*, 142091. [CrossRef]
88. Lothenbach, B.; Durdziński, P.; De Weerdt, K. Thermogravimetric Analysis. In *A Practical Guide to Microstructural Analysis of Cementitious Materials*; Scrivener, K., Snellings, R., Lothenbach, B., Eds.; CRC Press: Boca Raton, FL, USA, 2018; pp. 177–212. [CrossRef]
89. Zunino, F.; Lopez, M. Decoupling the Physical and Chemical Effects of Supplementary Cementitious Materi-als on Strength and Permeability: A Multi-Level Approach. *Cem. Concr. Compos.* **2016**, *65*, 19–28. [CrossRef]
90. Silva, Y.F.; Izquierdo, S.R.; Delvasto, S. Effect of Masonry Residue on the Hydration of Portland Cement Paste. *DYNA* **2019**, *86*, 367–377. [CrossRef]
91. Bernard, E.; Lothenbach, B.; Chlique, C.; Wyrzykowski, M.; Dauzères, A.; Pochard, I.; Cau-Dit-Coumes, C. Characterization of Magnesium Silicate Hydrate (M–S–H). *Cem. Concr. Res.* **2019**, *116*, 309–330. [CrossRef]
92. Liu, X.; Li, D.; Li, M.; Xie, H.; Yu, X.; Wang, H.; Wang, W.; Hong, J.; Zhang, Z.; Feng, P. Unraveling the Role of Magnesium Salts in Liquid Alkali-Free Accelerators: Insights into Setting and Early-Age Properties of Accel-erated Cement Pastes. *Cem. Concr. Res.* **2025**, *195*, 107920. [CrossRef]
93. Lee, S.T.; Hooton, R.D.; Kim, S.S.; Kim, E.K. Effect of Fineness of High-Alumina Ground Granulated Blast furnace Slag on Magnesium Sulphate Attack. *Mag. Concr. Res.* **2006**, *58*, 301–311. [CrossRef]
94. Sreenivasan, H.; Bernard, E.; Santos, H.S.; Nguyen, H.; Moukannaa, S.; Adediran, A.; Provis, J.L.; Kinnunen, P. A Critical Review of Magnesium Silicate Hydrate (M–S–H) Phases for Binder Applications. *Cem. Concr. Res.* **2024**, *178*, 107462. [CrossRef]
95. Baghabra Al-Amoudi, O.S. Attack on Plain and Blended Cements Exposed to Aggressive Sulfate Environments. *Cem. Concr. Compos.* **2002**, *24*, 305–316. [CrossRef]
96. Gu, Y.; Dangla, P.; Martin, R.P.; Omikrine Metalssi, O.; Fen-Chong, T. Modeling the Sulfate Attack Induced Expansion of Cementitious Materials Based on Interface-Controlled Crystal Growth Mechanisms. *Cem. Concr. Res.* **2022**, *152*, 106676. [CrossRef]
97. Bonen, D.; Cohen, M.D. Magnesium sulfate attack on portland cement paste-i. micro-structural analysis. *Cem. Concr. Res.* **1992**, *22*, 169–180. [CrossRef]
98. Sotiriadis, K.; Hlobil, M.; Viani, A.; Mácová, P.; Vopálenský, M. Physical-Chemical-Mechanical Quantitative Assessment of the Microstructural Evolution in Portland-Limestone Cement Pastes Exposed to Magnesium Sulfate Attack at Low Temperature. *Cem. Concr. Res.* **2021**, *149*, 106566. [CrossRef]

99. Hekal, E.E.; Kishar, E.; Mostafa, H. Magnesium Sulfate Attack on Hardened Blended Cement Pastes under Different Circumstances. *Cem. Concr. Res.* **2002**, *32*, 1421–1427. [CrossRef]
100. Fang, Z.; Wang, C.; Hu, H.; Li, Z.; Ran, B.; Zhou, S. Inhibition of Sulfate Attack on Cement-Based Materials under Stray Currents and Low Temperatures by Mineral Materials. *J. Build. Eng.* **2025**, *107*, 112750. [CrossRef]
101. Kunther, W.; Lothenbach, B.; Scrivener, K.L. Deterioration of Mortar Bars Immersed in Magnesium Contain-ing Sulfate Solutions. *Mater. Struct./Mater. Et Constr.* **2013**, *46*, 2003–2011. [CrossRef]
102. Bernard, E.; Lothenbach, B.; Cau-Dit-Coumes, C.; Pochard, I.; Rentsch, D. Aluminum Incorporation into Magnesium Silicate Hydrate (M–S–H). *Cem. Concr. Res.* **2020**, *128*, 105931. [CrossRef]
103. Jin, M.; Ma, Y.; Li, W.; Huang, J.; Zeng, H.; Lu, C.; Zhang, J.; Liu, J. Degradation of C–S–H(I) at Different De-calcification Degrees. *J. Mater. Sci.* **2022**, *57*, 19260–19279. [CrossRef]
104. Song, Y.; Wang, Y.; Wang, Y.; Liu, B. Experimental Study on Chloride Threshold Content in Reinforced Con-crete above and in Water Level Fluctuation Zone Considering Sulphate Attack. *Constr. Build. Mater.* **2025**, *475*, 141131. [CrossRef]
105. Ding, X.H.; Luo, B.; Zhou, H.T.; Chen, Y.H. Generalized Solutions for Advection–Dispersion Transport Equa-tions Subject to Time- and Space-Dependent Internal and Boundary Sources. *Comput. Geotech.* **2025**, *178*, 106944. [CrossRef]
106. Su, Y.; Luo, B.; Luo, Z.; Xu, F.; Huang, H.; Long, Z.; Shen, C. Mechanical Characteristics and Solidification Mechanism of Slag/Fly Ash-Based Geopolymer and Cement Solidified Organic Clay: A Comparative Study. *J. Build. Eng.* **2023**, *71*, 106459. [CrossRef]
107. Shi, T.; Li, K.M.; Wang, C.Z.; Jin, Z.; Hao, X.K.; Sun, P.; Han, Y.X.; Pan, C.G.; Fu, N.; Wang, H.B. Fracture Toughness of Recycled Carbon Fibers Reinforced Cement Mortar and Its Environmental Impact Assessment. *Case Stud. Constr. Mater.* **2025**, *22*, e04866. [CrossRef]
108. Sha, F.; Dong, Y.; Gu, S.; Fan, X.; Xiao, W. Study on Novel Alkali-Activated Cementitious Grout for Scour Control of Offshore Foundation. *Geomech. Energy Environ.* **2025**, *42*, 100663. [CrossRef]
109. Luo, B.; Su, Y.; Ding, X.; Chen, Y.; Liu, C. Modulation of Initial CaO/Al_2O_3 and SiO_2/Al_2O_3 Ratios on the Properties of Slag/Fly Ash-Based Geopolymer Stabilized Clay: Synergistic Effects and Stabilization Mecha-nism. *Mater. Today Commun.* **2025**, *47*, 113295. [CrossRef]

Disclaimer/Publisher's Note: The statements, opinions and data contained in all publications are solely those of the individual author(s) and contributor(s) and not of MDPI and/or the editor(s). MDPI and/or the editor(s) disclaim responsibility for any injury to people or property resulting from any ideas, methods, instructions or products referred to in the content.